Acta Biomaterialia 209 (2026) 504–520

Contents lists available at ScienceDirect

Acta Biomaterialia

journal homepage: www.elsevier.com/locate/actbio

Full length article

Magnetoelectric core-shell nanoparticles for nervous tissue electrostimulation: Performance in In vitro and ex vivo organotypic cultures

Maurizio Gulino [a,b,c], Donghoon Kim [d], Qiao Tang [d], Semih Sevim [d], Elric Zhang [d], Hao Ye [d], Xiang-Zhong Chen [d,e,f], Miguel Rafael Gonçalves Morais [a,b], Sofia Duque Santos [a,b], Salvador Pané [d,**], Ana Paula Pêgo [a,b,g,*]

[a] i3S - Instituto de Investigação e Inovação em Saúde, Universidade do Porto, R. Alfredo Allen 208, 4200-135 Porto, Portugal
[b] INEB - Instituto de Engenharia Biomédica, Universidade do Porto, R. Alfredo Allen 208, 4200-135 Porto, Portugal
[c] FEUP - Faculdade de Engenharia da Universidade do Porto, s/n, R. Dr. Roberto Frias, 4200-465 Porto, Portugal
[d] Multi-Scale Robotics Lab (MSRL), Institute of Robotics and Intelligent Systems (IRIS), ETH Zurich, Tannenstrasse 3, 8092, Zurich, Switzerland
[e] Institute of Optoelectronics, State Key Laboratory of Photovoltaic Science and Technology, Shanghai Frontiers Science Research Base of Intelligent Optoelectronics and Perception, Fudan University, Shanghai, 200433 PR China
[f] Yiwu Research Institute of Fudan University, 322000 Yiwu, China
[g] ICBAS – Instituto de Ciências Biomédicas Abel Salazar, Universidade do Porto, R. de Jorge de Viterbo Ferreira 228, 4050-313 Porto, Portugal

ARTICLE INFO

Keywords:
Magnetoelectric nanoparticles
Neural stimulation
Biocompatibility
Organotypic brain cultures
Nanoparticle magnetic guidance

ABSTRACT

This work presents functional multiferroic cobalt ferrite-based nanoparticles (CFO NPs) coated with calcium/zirconium-doped barium titanate (CFO-BCZT) that demonstrate notable magnetoelectric coupling and biocompatibility for neural applications. The core-shell structure was synthesized through hydrothermal and sol-gel processes. Uncoated CFO NPs and CFO NPs coated with bismuth ferrite (CFO-BFO) were used for comparison. X-ray diffraction revealed cubic CFO core and tetragonal BCZT shell without any secondary phase, nor impurities. Magnetoelectric coupling effect of CFO-BCZT MENPs was revealed through piezoresponse force microscopy. Biological cellular responses to CFO-BCZT MENPs were evaluated through cytotoxicity assays, microscopy analysis, and cellular uptake on primary neurons, astrocytes or microglia cultures. Long-term effects were studied in rodent 3D organotypic hippocampal cultures. Moreover, the magnetoelectric performance of CFO-BCZT and CFO-BFO MENPs was assessed in vitro with SH-SY5Y human neuronal cell lines under magnetic stimulation. The results showed CFO-BCZT MENPs superior biocompatibility both in vitro and ex vivo in organotypic brain slices, while CFO-BFO MENPs reduced microglial viability and induced inflammatory changes. Additionally, tissue penetration of CFO-BCZT MENPs through magnetic attraction was successfully achieved on organotypic hippocampal cultures, without causing either cell damage or disruption of neural connections. Finally, SH-SY5Y neuronal cell line showed good neurite outgrowth with the tested magnetic stimulation parameters. In conclusion, CFO-BCZT MENPs not only exhibited a magnetoelectric coupling effect but also greater biocompatibility compared to CFO-BFO and uncoated CFO NPs, positioning them as promising composite materials for brain stimulation therapies.

Statement of significance: Magnetoelectric nanoparticles are emerging as promising tools for non-invasive brain stimulation therapies. Our work introduces biocompatible multiferroic cobalt ferrite- based nanoparticles (CFO NPs) coated with calcium/zirconium-doped barium titanate (CFO-BCZT) as candidate materials for neural applications, representing a combination of cobalt ferrite cores with calcium/zirconium-doped barium titanate shells. These core-shell nanostructures exhibit strong magnetoelectric coupling and significantly improved biocompatibility compared to conventional alternatives, such as bismuth ferrite coatings. Their ability to penetrate brain tissue through magnetic attraction without inducing cellular toxicity or inflammation on ex vivo organotypic hippocampal slices, while promoting neurite outgrowth on in vitro neuronal cell cultures, positions

* Corresponding author at: i3S - Instituto de Investigação e Inovação em Saúde, Universidade do Porto, R. Alfredo Allen 208, 4200-135 Porto, Portugal.
** Corresponding author.
E-mail addresses: vidalp@ethz.ch (S. Pané), apego@i3s.up.pt (A.P. Pêgo).

https://doi.org/10.1016/j.actbio.2025.11.038
Received 22 July 2025; Received in revised form 31 October 2025; Accepted 20 November 2025
Available online 26 November 2025

them as promising tools for non-invasive neural modulation. This study paves the way for safe, wireless brain stimulation platforms using multifunctional nanomaterials.

1. Introduction

Transcranial magnetic stimulation (TMS) represents an effective, minimally invasive approach for treating several neurological dysfunctions [1,2]. Although TMS already has clinical translations and proven long-term safety, it is spatially limited and struggles to stimulate deep-brain areas [3].

Magnetoelectric nanoparticles (MENPs) are an emerging class of materials with distinct physicochemical properties and many biomedical applications, including non-invasive neuromodulation in the central nervous system [4]. MENPs are core-shell structures traditionally composed of a ferromagnetic core and a piezoelectric shell. This combination produces the magnetoelectric coupling effect, and external magnetic field gradients can guide the NPs through the body, even at deeper levels [5]. MENPs have been studied as drug nanocarriers for cancer therapy [6,7], targeted delivery of drugs across the blood-brain barrier (BBB), and controlled release in the brain parenchyma. Additionally, recent in vivo studies demonstrated successful non-invasive delivery of MENPs in the brain in rodent and non-human primate models [8,9]. One of the most promising applications of MENPs is within the context of deep brain stimulation (DBS), as they can generate localized electric fields from external magnetic stimuli. MENPs could represent a new generation of neurostimulators for DBS with several advantages over traditional implantable microelectrodes and TMS, specifically minimal invasiveness and high target specificity. In vivo studies on rodent animal models have already reported remote electrical polarization of MENPs with external magnetic fields and subsequent local modulation of neural activity in deep brain targets [10,11].

However, MENPs have currently been limited to the preclinical level. To speed their translation from bench to bedside, it is paramount to establish their safety and reliability for clinical use. Despite this, few studies have investigated the response of neuronal and glial cells to contact with the proposed MENPs and the impact of their motion through brain tissue. Moreover, limited knowledge is available regarding the potential long-term toxicity of the most widely employed materials for MENPs design, and rigorous diagnostic assessments are necessary before their broad deployment in clinical settings. Thus, a serious study on functional and biocompatible coatings and alternative NP materials is essential to meet the requirements for successful biomaterials.

In response to the growing interest in minimally invasive neurostimulation technologies, various core–shell magnetoelectric nanoparticles (MENPs) have been developed for DBS and neuromodulation. Towards this goal, several magnetic cores such as magnetite (Fe_3O_4), nickel ferrite ($NiFe_2O_4$), and manganese ferrite ($MnFe_2O_4$) have been explored for their lower magnetic anisotropy, reduced toxicity, and tunable magnetostrictive properties. Fe_3O_4-based MENPs have demonstrated wireless neural stimulation both in vitro and in vivo without inducing cytotoxicity [12,13], while $NiFe_2O_4$ and $MnFe_2O_4$ cores have been incorporated into core–shell architectures, where their soft magnetic character and biocompatibility contribute to efficient magnetoelectric coupling and functional bioactivation [14,15]. On the piezoelectric side, barium titanate ($BaTiO_3$) [16,17] has been investigated in combination with ferromagnetic cores to enable induction and inhibition of action potentials under alternating and direct magnetic fields in vitro, as well as to stimulate neural activity in vivo. Polyvinylidene fluoride (PVDF), a flexible piezoelectric polymer, is a versatile material as a coating or scaffold for magnetoelectric devices capable of inducing wireless modulation and recovery of motor behavior, as well as cell differentiation and tissue regeneration in vivo [12,18].

CFO is the most popular core material for MENPs, particularly for DBS, due to its chemical and thermal stability, good saturation magnetization, and high magnetostriction coefficient. Its strong magnetostrictive response enables efficient magnetoelectric coupling when paired with piezoelectric coatings, making it a preferred choice in preclinical neuromodulation studies [19,20]. Similarly, BFO is one of the most widely studied multiferroic materials thanks to its attractive electrical, magnetic, and piezoelectric properties. Thanks to its significant piezoelectric coefficient, BFO is a functional coating for magnetostrictive CFO as the basis for MENPs and nanomaterials for tissue electrical stimulation [21,22]. However, pre-clinical and clinical studies in the literature have reported the toxicity of BFO and bismuth compounds [23–27].

BCZT is another coating for CFO NPs known for its enhanced piezoelectric properties. This material offers remarkable advantages thanks to several key properties. It is highly biocompatible, showing low cytotoxicity toward human cells like osteoblasts and endothelial cells [28,29]. It is a lead-free, environmentally friendly alternative to traditional piezoceramics. It exhibits a higher piezoelectric response than $BaTiO_3$-based ceramics, allowing for generating high electric signals under mechanical stress [30]. Moreover, it displays strong electromechanical performance and thermal stability at body temperature, making it suitable for MENPs design and biomedical devices [31].

Previous studies have reported the synthesis of CFO-BCZT nanocomposites exhibiting magnetoelectric coupling properties [32–34]. However, those studies did not explore biocompatibility or application in biological systems.

In contrast, we present functional multiferroic core-shell MENPs of cobalt ferrite (CFO) coated with calcium, zirconium-doped barium titanate (CFO-BCZT) with ideal magnetoelectric coupling and biocompatibility for neural applications. Here, the proposed BCZT coatings for CFO cores are compared with BFO coatings in MENP design, performance, and cellular responses assessment (Fig. 1a–b). The synthesis of CFO-BCZT and CFO-BFO MENPs by hydrothermal and sol-gel processes and their structure and magnetoelectric performance characterization are described. In addition to performing traditional short-term in vitro primary cell cultures, we assess long-term biocompatibility on a complex and relevant 3D system - the rodent organotypic hippocampal cultures [35–37](Fig. 1c–d). We also employ organotypic hippocampal cultures to explore the impact of MENPs motion in terms of tissue viability and neuronal network integrity, 24 h after external magnetic field application. This expands upon previous studies that have primarily considered the functional ability of MENPs to cross the BBB or the effect of their movement and presence on brain tissue [38] and hippocampal slices [39] (Fig. 1e). Finally, we test magnetic stimulation on human neuronal cell lines using both CFO-BCZT and CFO-BFO MENPs (Fig. 1f). Altogether, this study links biomaterial's structure and function to biomaterials development for neurological applications.

2. Materials and methods

All reagents were acquired from Sigma Aldrich with chemical grade unless otherwise stated.

2.1. Synthesis of CFO core NPs

Single crystalline CFO core NPs were synthesized using co-precipitation and hydrothermal methods, as previously described [40,41]. 2 g of acetyltrimethylammonium bromide was dissolved in 30 mL of deionized (DI) water, and then 1 g of iron(III) chloride hexahydrate and 0.24 g of cobalt(II) chloride anhydrous powders were dissolved.

Subsequently, 6 M of an aqueous sodium hydroxide solution was mixed with the previous solution (co-precipitation). Synthesized CFO NPs were collected and washed with DI water, acetone, and ethanol.

2.2. Synthesis of CFO-BFO core-shell MENPs

The BFO shell was synthesized by sol-gel process as previously described [40,41]. 0.243 g of iron(III) nitrate nonahydrate and 0.322 g of bismuth(III) nitrate pentahydrate were dissolved in 60 mL of ethylene glycol solution and mixed with 0.1 g of CFO NPs. The solvent was evaporated overnight at 80 °C, and the dried powder was annealed at 600 °C for 2 h.

2.3. Synthesis of CFO-BCZT core-shell MENPs

BCZT shell was synthesized by sol-gel process. Firstly, 2.45 mL of titanium(IV) butoxide (97 wt. %, and 0.37 mL of zirconium(IV) butoxide solution (80 wt.) were added dropwise to a solution of 10 mL 2-methoxyethanol and 1 mL acetylacetone (solution A). 1.736 g of barium acetate and 0.211 g of calcium acetate were dissolved in 5 mL of glacial acetic acid at 60 °C and mixed with solution A after natural cooling to room temperature (solution B). 75 mg of CFO NPs dispersed in 0.33 mL of DI water was added to 3.3 mL of solution B. After stirring for 1 h, the solvent evaporated overnight at 80 °C, and then the resulting particles were annealed at 900 °C for 2 h.

2.4. Characterization of the MENPs

The crystallinity of CFO-BCZT and CFO-BFO MENPs was analyzed with an X-ray diffractometer (Bruker AXS D8 Advance). Transmission electron microscopy (TEM), high-angle annular dark-field scanning transmission electron microscopy (HAADF-STEM), and energy dispersive X-ray spectroscopy (EDX) were performed with FEI Talos F200X. To analyze the piezoelectric and magnetoelectric properties of core-shell MENPs, piezoresponse force microscopy (NT-MDT) equipped with an in-plane DC magnetic field setup was employed. The local piezoelectric hysteresis loop was measured by applying a DC voltage superimposed with a small AC voltage between the Au-coated conductive tip and the Au-coated substrate. The local hysteresis loops were measured and averaged over 5 times.

2.5. Animals

All animal procedures were pre-approved by the i3S Ethics Committee (CEA, i3S). All the experiments were performed according to institutional ethical guidelines (i3S), the National law (DL 113/2013),

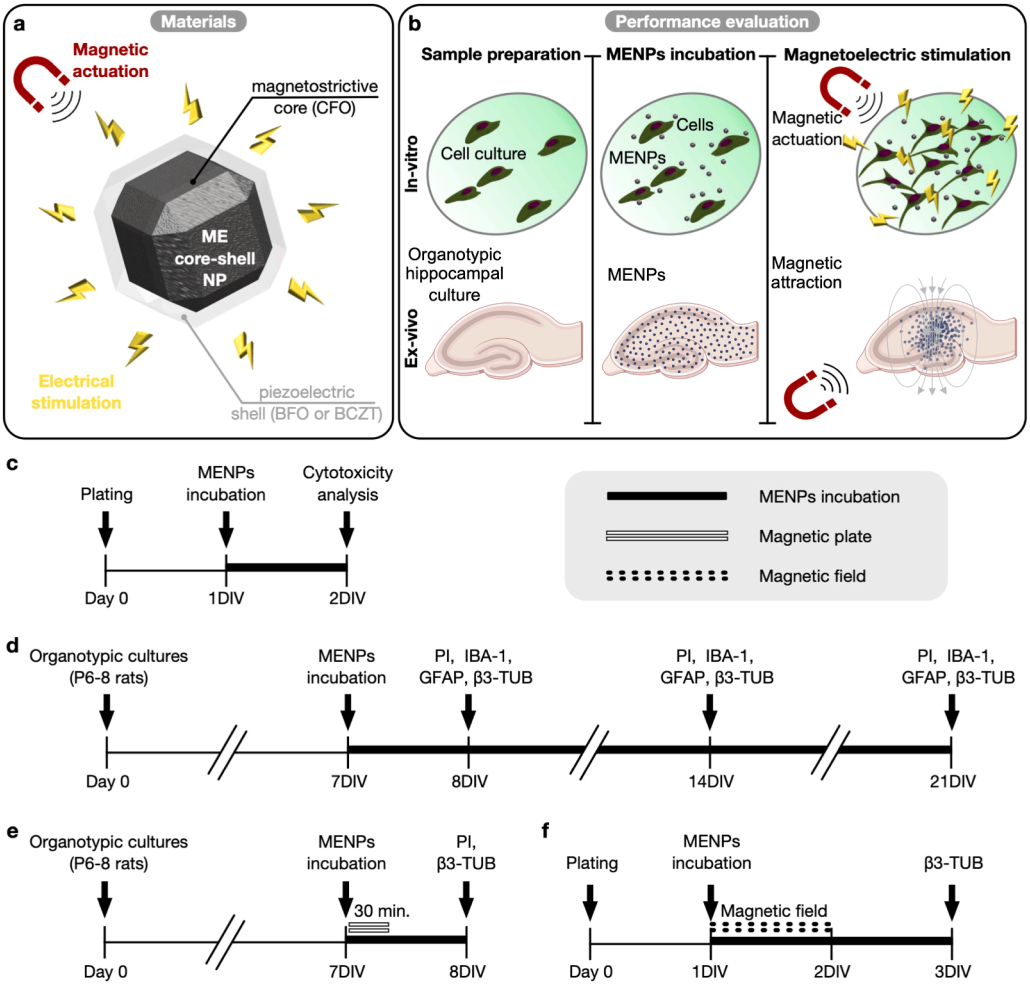

Fig. 1. a-b) Schematic representation of **a)** core-shell magnetoelectric nanoparticles (MENPs), and **b)** the in vitro and ex vivo performance evaluation for magnetoelectric stimulation. **c-d)** In vitro and ex vivo experimental study designs representing the experimental schemes for investigating the biocompatibility of MENPs in **c)** in vitro primary neuronal and glial cells and **d)** ex vivo rat hippocampal organotypic slices, as well as the experimental schemes **e)** for studying the impact of MENPs motion on ex vivo organotypic cultures and **f)** for investigating the in vitro performance of MENPs in magnetoelectric stimulation of neuronal cells. Abbreviations: DIV: days in vitro; PI: propidium iodide fluorescence staining; IBA-1: ionized calcium binding adaptor molecule 1 immunofluorescence staining; GFAP: Glial fibrillary acidic protein immunofluorescence staining; β3-TUB: β3-tubulin immunofluorescence staining.

and European Union guidelines (EU Directive 2010/63/EU for animal experiments) with maximal care to minimize animal suffering, as well as the number of animals used. Only authorized and experienced researchers performed animal experimentation. The rats or mice were kept in an enriched housing environment with ad libitum feed and water supply. They were kept under a 12 h light/12 h dark cycle at the i3S animal facility, with controlled ambient temperature and humidity.

Wistar Han rat pups, males and females, 0–2 days old, were used to obtain primary microglia and astrocytes isolated from brains. Wistar Han rat pups, males and females, 6–8 days old, were used to prepare the hippocampal slice cultures. C57BL/6 mice embryos (E16.5) were used to obtain primary mouse neuronal cortical cell cultures (NCCC).

2.6. Primary microglia and astrocyte cultures

Primary cultures of microglia and astrocytes were obtained from P0-P2 rat pups, as previously described, with some modifications [42,43]. Briefly, cortices were isolated and digested in Hank's Balanced Salt Solution (HBSS, Gibco, Life Technologies) without Ca^{2+}, $Mg^{2+,}$ and supplemented with trypsin (0.0025 % (w/v), Gibco, Life Technologies) and 0.001 mg/mL DNAse I (Applichem LifeSciences) for 15 min at 37 °C. Dissociated cortices were cultured in 10 μg/mL poly(L-lysine) (PLL) coated 75 cm^2 flasks (BioLite) and maintained in Dulbecco's Modified Eagle Medium (DMEM, Gibco, Life Technologies) supplemented with 10 % (v/v) heat-inactivated (30 min, 56 °C) fetal bovine serum (FBS, Gibco, Life Technologies) and 1 % (v/v) penicillin-streptomycin (P/S, Biowest). When confluence was reached (~12 days), the flasks were shaken for 2 h (200 rpm, 37 °C, 5 % CO_2) on an orbital shaker to obtain the cells that detach - microglia. Subsequently, an additional overnight shake (220 rpm, 37 °C, 5 % CO2) was carried out to remove other loosely attached cells - microglia and oligodendrocyte progenitor cells. This process was repeated once a week for three weeks. The remaining cells were mainly astrocytes that were further trypsinized (0.025 % (w/v) trypsin-EDTA, Gibco, Life Technologies) at 37 °C for 5 min to increase cell purity.

Primary microglia were incubated in DMEM Nutrient Mixture F-12 (Gibco, Life Technologies) supplemented with 10 % (v/v) heat-inactivated FBS and 1 % (v/v) Penicillin-Streptomycin (PS) antibiotics and plated in 10 μg/mL poly(D-lysine) (PDL) coated CellCarrier Ultra 96-well microplates (Perkin-Elmer) at a concentration of $30 \times 10^{\wedge 4}$ viable cells (trypan blue assay) per well in 100 μL. Similarly, primary astrocytes (90 % purity) were plated into uncoated 96-well microplates at a concentration of $9.6 \times 10^{\wedge 3}$ viable cells per well in 100 μL of DMEM supplemented with 10 % (v/v) heat-inactivated FBS and 1 % (v/v) PS. Both cell types were maintained at 37 °C with 95 % O_2 and 5 % CO_2 for 24 h until further use.

2.7. Cortical neuron cultures

Primary mouse neuronal cortical cell cultures (NCCC) were prepared from E16.5 C57BL/6 mice embryos according to a previously reported protocol with some modifications [44]. Briefly, cortices were digested with trypsin (1.5 mg/mL), washed with HBSS containing 10 % (v/v) FBS, and then washed only with HBSS to remove FBS. The tissue was then mechanically dissociated in Neurobasal medium (NBM; Gibco, Life Technologies) using a pipette, and cells were filtered and counted (95 % purity). Cells were then plated in 50 μg/mL PDL coated 96-well microplates at a concentration of $15 \times 10^{\wedge 4}$ viable cells per well in a total volume of 300 μL of NBM supplemented with 2 % (v/v) NeuroCult™ SM1 Neuronal Supplement (StemCell Technologies), L-glutamine (0.5 mM), L-glutamic acid monosodium salt hydrate (0.025 mM) and gentamycin (50 μg/mL, Gibco, Life Technologies) at 37 °C with 5 % CO_2, for 7 days until further use.

2.8. Live-dead assay

Primary cortical neurons, microglia, and astrocytes were incubated with the MENPs at a concentration of 10 and 100 μg/mL for 24 h (Fig. 1c). Subsequently, Calcein AM cell permeant (Molecular Probes) and Hoechst 33,342 (Anaspec) were added in the medium in each well at a final concentration of 1 μM and 20 μM, respectively, for 20 min. Finally, cells were incubated with propidium iodide (PI) at a concentration of 1.5 μM for additional 5 min. As positive controls for all the cells, 0.01 % (v/v) Triton X-100 was added to the medium to induce cell death, 10 min before incubation with the fluorescent dyes. Finally, cells were imaged using an INCell Analyzer 2000 (GE Healthcare) for high-throughput analysis.

2.9. Reactive oxygen species (ROS) and nitrite oxide (NO) quantification

CellROX™ Deep Red Reagent (Invitrogen) was employed to detect ROS production by primary microglia, according to the manufacturer's instructions. Briefly, after 24 h incubation with MENPs, CellROX Deep Red Reagent was added to the incubation medium at a final concentration of 5 μM for 30 min. Then, cells were immediately imaged using an INCell Analyzer 2000. Cells incubated for 3 h with 100 μM menadione diluted in the cell culture medium before ROS quantification were used as positive control.

NO production by microglia was measured using the Griess Reagent detection method as previously described [45]. After incubating with MENPs for 24 h, 100 μL of supernatant was transferred into a 96-well plate and mixed with equal volumes of Griess reagent for 1 h at room temperature (RT). Subsequently, absorbance was measured with a Bio-Tek Synergy Mx Monochromator-Based Multi-Mode Reader (Agilent) at a wavelength of 550 nm. Lipopolysaccharide (LPS) was used as a positive control in the incubation medium at a 200 ng/mL concentration in 0.1 M phosphate-buffered saline (PBS) for 24 h.

2.10. Prussian blue staining

We employed the Prussian blue staining in microglia as previously described [46]. Briefly, after incubation with MENPs at 10 μg/mL for 24 h, cells were washed twice with PBS and fixed in 4 % (w/v) paraformaldehyde (PFA) in PBS for 15 min. After PFA removal, cells were incubated with Perl's reagent composed of equal amounts (1:1, v/v) of 4 % (w/v) potassium ferrocyanide in DI water and 12 % (w/w) aqueous hydrochloric acid solution (HCl) for 30 min. Subsequently, cells were washed three times with DI water, counterstained with 0.1 % (w/v) Nuclear Fast Red solution in DI water for 5 min, followed by three washes with DI water and immediately imaged.

2.11. Organotypic hippocampal slice cultures

Rodent Organotypic hippocampal slice cultures were established using the previously described interface method [35,37]. Briefly, 400 μm slices obtained from the hippocampus of rat pups' brain, were placed into 0.4 μm Millicell® PTFE culture inserts (Merck-Millipore) in 6-well plates (Corning) and maintained at 37 °C with 5 % CO_2 and 95 % atmospheric air for 7 days. 1 mL of incubation medium composed of Opti-MEM™ (Gibco, Life Technologies) based medium supplemented with 25 % (v/v) heat-inactivated horse serum (HS, Gibco, Life Technologies), 25 % (v/v) HBSS, D-(+)-glucose 25 mM, and 1 % (v/v) PS was placed in each well. Medium was changed 24 h after the plating and then every 2 days.

MENPs administration was carried out at 7 days in vitro (DIV) using a Narishige Pneumatic Microinjector (Model IM-300) connected to a nitrogen cylinder as previously described [35]. Inserts with the brain slices were transferred into a petri dish with 3 mL of warm incubation medium. 400 ng of MENPs suspended in 1 M HEPES buffer (Gibco, Life Technologies), at a concentration of 2 mg/mL, were first sonicated for 1 min in a sonication bath, then loaded into glass microcapillaries (WPI 1B200F-4, with Filament) and inserted in a three-dimensional manipulator. 12–15 drops were deposited on the cornu Ammonis (CA) 3, CA1,

and dentate gyrus (DG) areas without damaging the tissue. In control slice cultures, HEPES buffer was deposited in the same way. The procedure was performed in sterile conditions inside a laminar flow hood equipped with a KL300 stereomicroscope (Leica). After MENPs administration, inserts were placed in the well plates with fresh pre-heated medium. Subsets of slice cultures were analyzed at 8 DIV, 14 DIV, and 21 DIV (corresponding to 1day, 7 days, and 14 days in contact with the MENPs) (Fig. 1d).

2.12. Motion experiments of MENPs in brain slices

The impact of CFO-BCZT MENPs' motion was assessed on organotypic hippocampal slice cultures. Briefly, 400 ng of CFO-BCZT were administered on a subset of cultures 7 days after plating. Then, a magnetic plate for magnetofection (10,000 Oe, OZ Biosciences) was placed at the bottom of the 6-well plate containing the insert and left in the incubator for 30 min to allow motion of the MENPs from the top of the slices inwards. Subsequently, the magnetic plate was removed, and slices were kept in the incubator for 24 h (Fig. 1e). The impact of MENPs' motion in the brain tissue was assessed by PI uptake and β3-tubulin immunofluorescence. Moreover, MENPs' penetration and tissue integrity were also evaluated by confocal and TEM imaging on slice cryosections.

2.13. Propidium iodide assay in brain slices

PI uptake was performed to assess the impact of MENPs on organotypic hippocampal slice cultures as previously described [35]. The assay was performed at 8 DIV, 14 DIV, and 21 DIV (1 day, 7 days, and 14 days after MENPs administration, respectively). PI was added to the culture medium for 1 h at a concentration of 6 μM. Slices treated with 0.1 % (v/v) Triton X-100 in PBS for 1 h before PI administration were used as positive controls. Each membrane insert was gently cut out and placed inside a 35 mm imaging μ-dish (ibidi) for visualization.

2.14. Immunofluorescence

In organotypic hippocampal slice cultures, at the end of the 3 above-described time points (Fig. 1d), the medium was removed from each well and inserts were washed with pre-warmed PBS for 2 times, followed by fixation of the slices with 4 % (w/v) PFA at room temperature (RT) for 1 h. Slices still attached to the membrane were individually cut out and incubated in permeabilization/blocking buffer composed of 1 % (w/v) bovine serum albumin (BSA), 5 % (v/v) heat-inactivated FBS, and 1 % (v/v) Triton X-100 in PBS overnight at 4 °C with gentle shaking. After PBS washing, slices were incubated with rabbit anti-ionized calcium binding adaptor molecule 1 (Iba-1, 1:800, Wako Chemicals), mouse anti-β3-tubulin (1:500, Promega) and rabbit anti-glial fibrillary acidic protein (GFAP, 1:500, Abcam) diluted in blocking buffer containing 1 % (w/v) BSA, 5 % (v/v) FBS, and 0.3 % (v/v) Triton X-100 in PBS for 48 h at 4 °C with gentle shaking. Slices were rewashed with 0.05 % (v/v) Triton X-100 in PBS at RT with gentle shaking. After primary antibody incubation, slices were incubated with Alexa Fluor 488 rabbit anti-goat IgG ($H + L$) secondary antibody (1:1000, Invitrogen) and Alexa Fluor 647 donkey anti-mouse IgG ($H + L$) secondary antibody (1:1000, Invitrogen) in blocking buffer for 3 h at RT with gentle shaking and then rewashed with 0.05 % Triton X-100 in PBS at RT with gentle shaking.

Nuclei were stained with Hoechst 33,342 solution (1 μg/mL, Thermo Fisher Scientific) in PBS for 30 min. Slices were placed on glass slides for mounting, as previously described, using a bridge mounting technique to preserve slices' integrity [35]. The samples were mounted with homemade Mowiol/glycerol (3:1), cover slipped, and stored in the dark at 4 °C until further use.

To prepare cryosections, slices were incubated at 4 °C overnight in PBS in 30 % (w/v) sucrose solution after PFA fixation. Then, slices were immersed in optimal cutting temperature embedding matrix (OCT, Fisher Scientific), frozen in liquid nitrogen, and immediately stored at −20 °C till further use. 20 μM transversal Cryosections were obtained using a CM1900 1 1 cryostat (Leica) and placed on glass slides. Nuclei were counterstained with 1 % fast nuclear red solution for 5 min and mounted using the homemade Mowiol/glycerol mounting medium described above.

2.15. TEM image analysis

For the ultrastructure analysis of the tissue and MENPs, organotypic hippocampal slice cultures were fixed in a solution of 2.5 % (w/v) glutaraldehyde (Electron Microscopy sciences) with 2 % (w/v) formaldehyde (Electron Microscopy sciences) in 0.1 M sodium cacodylate buffer at pH 7.4 for 1 h, at RT, and post fixed in 1 % w/v osmium tetroxide (Electron Microscopy Sciences) diluted in 0.1 M sodium cacodylate buffer. Slices were resuspended in HistogelTM (Thermo, HG-4000–012) and then stained with aqueous 1 % (w/v) uranyl acetate solution overnight, dehydrated, and embedded in Embed-812 resin (Electron Microscopy Sciences). Ultra-thin longitudinal hippocampal slice sections (50 nm thickness) were cut on an RMC Ultramicrotome (PowerTome, USA) using Diatome diamond knives. Sections were then mounted on mesh copper grids (Electron Microscopy Sciences) and stained with uranyl acetate substitute (Electron Microscopy Sciences) and lead citrate (Electron Microscopy Sciences) for 5 min each.

2.16. Magnetic stimulation using MENPs on SH-SY5Y neuronal cells

To investigate the effect of the MENPs after magnetic stimulation, we employed SH-SY5Y human neuronal cell line. For this experiment, CFO core-shell NPs with a thicker BCZT coating (15 ± 5 nm) were used, in parallel with CFO core-shell NPs with BFO coating. SH-SY5Y cells were obtained from Leibniz Institute, DSMZ-German Collection of Microorganisms and Cell Cultures GmbH. Cells were cultured in T75 flasks with DMEM GlutaMAX™ Supplement (Gibco, Life Technologies) with 15 % (v/v) FBS and 1 % (v/v) PS. The cells were maintained in culture for up to 5 passages at 37 °C with 95 % Oxygen and 5 % CO_2 until experiments. Cells were plated in PhenoPlate™ 96-well microplates at a density of 2.4 × 10^4 cells per well in 200 μL of high glucose GlutaMAX™ Supplement with 15 % (v/v) FBS, 1 % (v/v) PS, and 10 μM Retinoic acid. After 24 h, cells were incubated with MENPs diluted in the medium at 10 or 100 μg/mL. The plate was inserted in a custom-built electromagnetic setup generating the AC signal for magnetic stimulation, as previously described [22]. The magnetic field strength employed was 17,7 mT (1.5 kHz). Cells were stimulated for 24 h at 37 °C with 95 % O_2 and 5 % CO_2, followed by an additional 24 h without magnetic stimulation.

As described above, cells were fixed for in vitro cell cultures to assess the neurite outgrowth by MENPs after magnetic stimulation. Subsequently, cells were first permeabilized with 0.2 % (v/v) Triton X-100 in PBS for 15 min at RT, followed by incubation with blocking buffer composed of 5 % (w/v) BSA in PBS for 1 h at RT. After PBS washing, cells were incubated with mouse anti-β3-tubulin (1:500, Promega) diluted in blocking buffer containing 2 % (w/v) BSA, in PBS for 24 h at 4 °C with gentle shaking. After 2 washes in PBS at RT with gentle shaking, cells were incubated with Alexa Fluor 488 donkey anti-mouse IgG ($H + L$) secondary antibody (1:1000, Invitrogen) in blocking buffer for 1 h at RT with gentle shaking and protected from light. After 2 washes in PBS at RT for 5 min, cells were incubated with PhenoVue Hoeschst 33,342 (1:100 000, Perkin Elmer) for 10 min at RT. Cells were washed with PBS and imaged.

2.17. Image analysis and quantification

High-throughput live/dead analysis of microglia, astrocytes, and neurons incubated with MENPs at 10 and 100 μg/mL for 24 h was carried out with the INCell Analyzer 2000 platform (GE Healthcare) using a 20X objective. Dead cells, total cell number, and area were

quantified using the INCELL developer toolbox software (version 1.9, GE Healthcare).

For the quantification of MENPs internalization by microglia, a Zeiss Axiovert 200 M inverted fluorescence microscope with brightfield and 40X objective was used. The cell content of MENPs in every cell was quantified using ilastik software (version 1.3.3) and Image J software (version 1.53; National Institutes of Health, United States).

For image acquisition of PI uptake and immunofluorescence intensity quantification of Iba-1, GFAP, and β3-tubulin, a Zeiss Axiovert 200 M inverted fluorescence microscope equipped with 488, 565, and 647 nm filters was used. Images were acquired using a 5X objective. ImageJ software was employed to analyze and quantify fluorescence intensity on consistently selected regions of interest in CA3, CA1, and DG districts on each brain slice.

Immunofluorescence image acquisition of Hoechst, Iba-1, GFAP, and β3-tubulin in the organotypic hippocampal cultures was performed using a Leica Scanning Confocal SP8 equipped with 405, 488, and 633 filters (Leica Microsystems, Germany), composed of an inverted microscope Leica DMI8 (Leica Microsystems, Germany) and LAS X software (Leica Microsystems, Germany).

For the image acquisition of GFAP and β3-tubulin structures in the organotypic hippocampal cultures, images were acquired using a 63X objective, with confocal image stacks of 512×512 pixels, 16-bit depth, pixel size 0.63 μm, and zoom 0.75. Quantification was performed using the skeletonization tool on the ImageJ Software.

For the reconstruction of microglial cell morphology, images were acquired using a 63X objective, with confocal 16-bit depth image stacks of 1024 × 1024 pixels, with a pixel size of 0.334 μm and a zoom set at 0.75. Single cells with complete and defined processes were selected and imaged for analysis. Quantification of morphology was performed using the skeletonization tool on the ImageJ Software. The cell soma area, the number of processes, and the number of end points and junctions were calculated per cell.

For the quantification of MENPs' motion and penetration into the brain tissue after the application of the magnetic field, images of tissue cryosections were acquired with a Zeiss Axiovert 200 M inverted fluorescence microscope with a 63X objective equipped with a digital camera. Quantification was performed using ImageJ software by drawing a line from the detected MENPs into the tissue to the top side of the brain slice. To further confirm the differences between control groups, confocal images of Hoechst-stained brain slices with MENPs were acquired with a Leica Scanning Confocal SP8 equipped with 405 and brightfield filters, followed by 3D reconstruction using Imaris Software (version 9.5; Oxford Instruments, United Kingdom).

For the ultrastructure analysis of brain tissue and MENPs, images were viewed on a JEOL JEM 1400 transmission electron microscope (JEOL, Tokyo, Japan) and digitally recorded using a CCD digital camera Orius 1100 W (Tokyo, Japan).

For the high-throughput analysis of neurites in SH SY5Y cells, images were acquired with the Operetta CLS high-content analysis system (Perkin Elmer) equipped with a fully automated widefield (8 LED) fluorescence microscope and using a 0.4 20X water objective. Digital image analysis processing, segmentation, and quantification were performed using Harmony® software. The workflow pipeline was implemented using the "Find Nuclei" building block, detecting Phenovue Hoechst 33,342 staining. This was followed by segmentation of the neurites with the "Find Neurites" building block, measuring the related outgrowth parameters based on β3-tubulin immunofluorescence.

2.18. Statistics

Data from three independent experiments were presented as the mean ± standard error of the mean (SEM). Tukey's test after one-way analysis of variance (ANOVA) was used for statistical analysis. Data from the high-content analysis were presented as the mean ± standard deviation (STDEV) from triplicate wells. Data analysis and visualization were done using GraphPad Prism 9 (GraphPad Software, San Diego, CA, United States).

3. Results

3.1. Synthesis and characterization of MENPs

Magnetoelectric CFO-BCZT core-shell MENPs were proposed here as functional multiferroic core-shell MENPs. These were prepared using hydrothermal and sol-gel methods. CFO NPs coated with BFO (CFO-BFO MENPs), one of the most widely studied multiferroic coating materials [47], were compared with the corresponding coated sample.

Since CFO has a significant magnetostriction coefficient (max. 600 ppm) [48,49], this material was chosen as the magnetostrictive core material and synthesized using co-precipitation and hydrothermal methods. Piezoelectric BCZT and BFO shell materials were then coated over the CFO core NPs. The crystalline structures of CFO-BFO and CFO-BCZT core-shell MENPs were analyzed by X-ray diffraction (Fig. 2a, c), which confirmed a cubic Fd-3 m space group of CFO core NPs, a hexagonal R3c BFO shell, and a tetragonal P4mm BCZT shell without any secondary phase or impurities. Additionally, Rietveld refinement of the cores determined crystallite size to be within 40 ± 1 nm with a microstrain of 0.00162 ± 0.00002 (Supplementary Fig. 1). HAADF-STEM and EDX images further prove the core-shell structure of CFO-BFO (Fig. 2b) and CFO-BCZT (Fig. 2d) MENPs with core particles containing Co, Fe, and shells containing Bi, Fe for BFO (Fig. 2b (ii)-(iii)) and Ba, Zr, Ca, Ti for BCZT (Fig. 2d (ii)-(iii)). The size of the CFO core NPs is 35 ± 8 nm, in agreement with sizes calculated from the Rietveld refinement of the XRD patterns. The thickness of the BFO shell is around 2 ± 1 nm, while thin and thick BCZT shells are around 2 ± 1 nm and 15 ± 5 nm, respectively, as determined by HAADF-STEM images. These measurements are an estimate of a population of NPs measured via TEM, and accordingly, are not a measurement of the entire sample.

Magnetoelectric properties of both core-shell MENPs were characterized by local piezoelectric hysteresis loops measured by the PFM with or without magnetic fields (Fig. 3a–d). Under a 500 Oe DC in-plane magnetic field, both CFO-BFO and CFO-BCZT MENPs showed noticeable shifts in their coercive voltages (Fig. 3b and 3d, respectively), characteristic of magnetoelectric coupling. For CFO-BFO MENPs (Fig. 3b), positive and negative coercive voltages shifted from 3.18 V to 2.33 V and −1.34 V to −1.91 V, respectively. For CFO-BCZT MENPs (Fig. 3d), positive and negative coercive voltages shifted from 1.21 V to 1.76 V and −3.04 V to −3.32 V, respectively. In both cases, we also observed an asymmetric bias in the PFM butterfly loops typical of strained piezo layers, which was modified by applying the magnetic field, another key characteristic of magnetoelectrics. Using the calculation method from previous works [40,41], this corresponded to magnetoelectric coefficients of 2.84 × 10^{-6} mV cm^{-1} Oe^{-1} and 0.68 × 10^{-6} mV cm^{-1} Oe^{-1} for the BFO and BCZT shells, respectively. This matches with previously reported values for CFO-BFO core-shell composites [40]. It is important to note that estimates of magnetoelectricity from PFM measurements are only proof of a magnetically induced change in polarization behavior at the single NP scale and may vary from the collective effects of NP ensembles in biological conditions.

3.2. Impact of magnetostrictive core and ME core-shell MENPs on neural cell viability

MENPs cytotoxicity was first evaluated by exploring different neural cell cultures – cortical neurons, astrocytes, and microglia, with a high-throughput live/dead assay using the INCELL analyzer. These cells were selected to mimic the main cell types the NPs would encounter when administered in the brain. After incubation with CFO-BCZT, uncoated CFO and CFO-BFO MENPs at 10 and 100 μg/mL for 24 h (Fig. 1c), we observed that neuronal and astrocytes' viabilities were not affected (Fig. 4a–b and 4c-d, respectively). The Calcein/ PI was kept unchanged

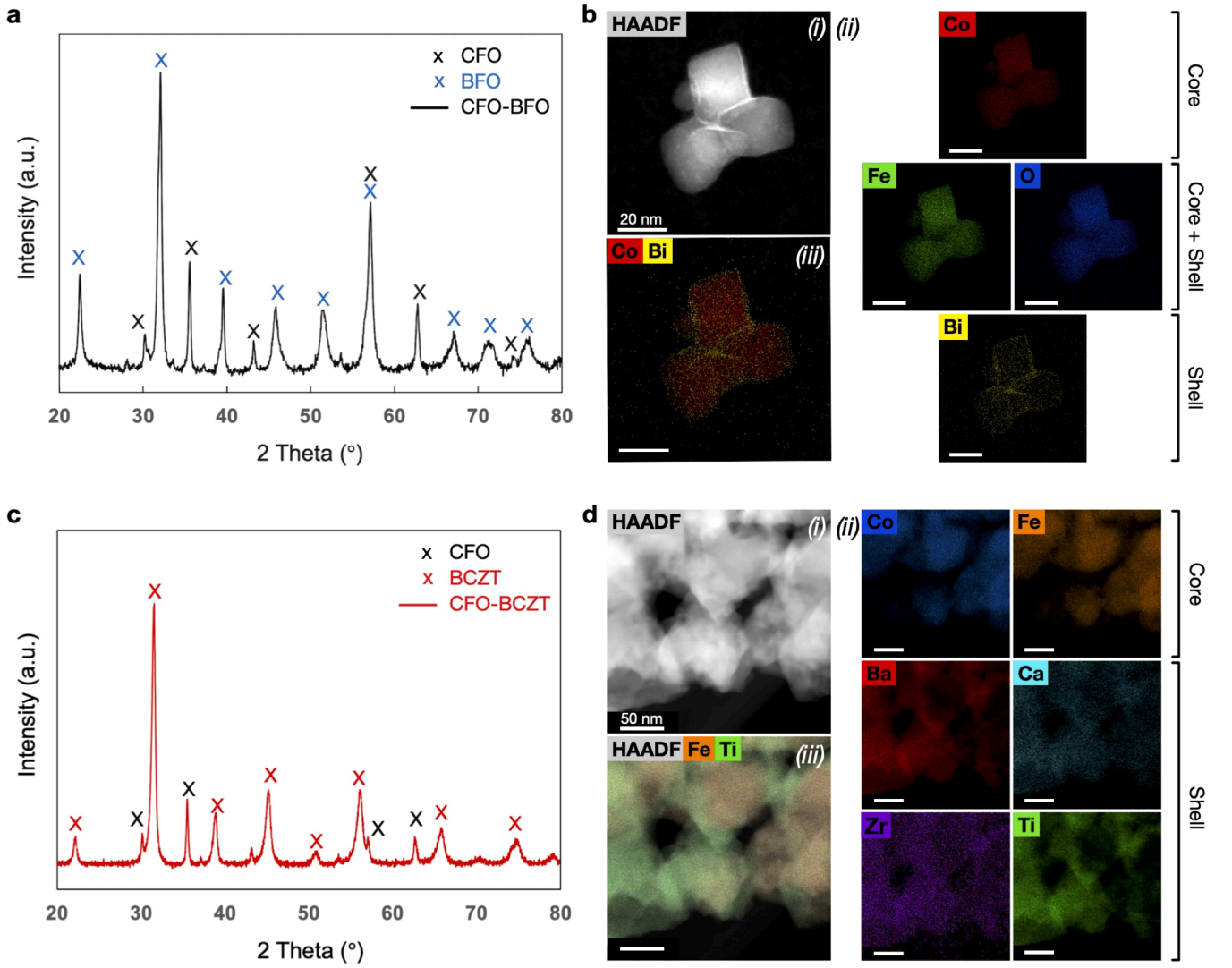

Fig. 2. Characterization of core-shell MENPs, including **a-b)** CFO-BFO and **c-d)** CFO-BCZT. **a, c)** X-ray diffraction data showing the crystallinity of CFO-BFO and CFO-BCZT MENPs, respectively. **b, d)** High-resolution transmission electron microscopy (TEM) analysis to demonstrate the core-shell nanoarchitecture of CFO-BFO and CFO-BCZT, respectively. TEM data represent the *(i)* high-angle annular dark-field scanning transmission electron microscopy (HAADF-STEM) images as well as energy dispersive X-ray spectroscopy (EDX) maps for representative *(ii)* core and shell elements, and *(iii)* their overlay.

in these two cell types after contact with the uncoated or coated NPs at low and high concentrations and for 24 h. In contrast, at high concentrations (100 μg/mL), primary microglia viability (Fig. 5a) was significantly compromised by CFO-BFO MENPs (Fig. 5b). Moreover, we observed significant microglia cell shrinkage and a decrease in cell adhesion (Fig. 5c and 5d, respectively) in cells incubated with uncoated CFO NPs at 100 μg/mL. The differential response of microglia reflects these cell types' unique roles and characteristics in mediating neuroinflammation. As the resident immune cells of the brain tissue, microglia are susceptible to environmental changes caused by foreign materials or stressors. This selective cytotoxicity suggests that the composition or surface properties of uncoated CFO and CFO-BFO MENPs may disrupt cellular homeostasis and functionality, leading to a transition to a pro-inflammatory state, where microglia attempt to alter their morphology and detach from the well plate. In contrast, neurons and astrocytes might possess more robust protective mechanisms or lower sensitivity to these NPs.

Despite these findings, we observed no ROS and NO production increase in microglia at the above-described conditions for all the NPs tested (Fig. 5e–f). The absence of increased ROS and NO production (Fig. 5e–f) suggests that the cytotoxicity observed might not be driven by oxidative stress, but could involve other mechanisms, such as altered cytoskeletal dynamics or disruption of cell-cell interactions, which are critical for microglial function. This aligns with findings in the literature where exposure to specific nanomaterials has been shown to induce stress responses that affect cell behavior, leading to altered morphology, reduced migration, and impaired viability [35,50–53]. Prussian blue staining that marks iron was employed to assess MENPs internalization and evaluate potential correlations between internalization and cytotoxicity. Image analysis and quantification using ImageJ software revealed that CFO-BCZT and CFO-BFO MENPs are less internalized by microglia when compared to CFO NPs (Fig. 6a–c). These data suggest that the BFO and BCZT shells make the NPs less prone to microglia phagocytic activity.

Nevertheless, despite this lower internalization, CFO-BFO MENPs displayed higher cytotoxicity at elevated concentrations. This underscores the need for further investigation into the specific interactions between microglial cells and these NPs. These data suggest that the BFO and BCZT shells make the NPs less prone to microglia phagocytic activity when compared to control CFO NPs. Most significantly, CFO-BCZT MENPs displayed the best biocompatibility, with no signs of toxicity at higher concentrations.

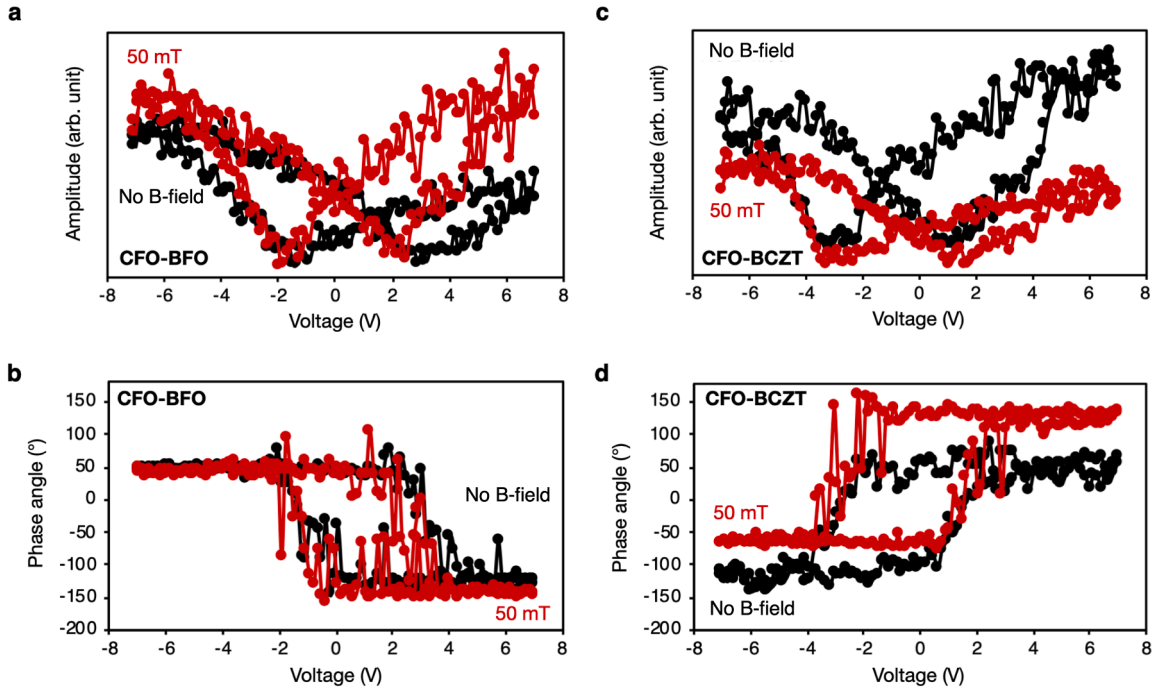

Fig. 3. Piezo force microscopy (PFM) measurements on different types of core-shell MENPs, including **a-b)** CFO-BFO and **c-d)** CFO-BCZT. The curves show the local **a, c)** amplitude and **b, d)** phase hysteresis loops that are obtained with (red) and without (black) applied external field (50 mT).

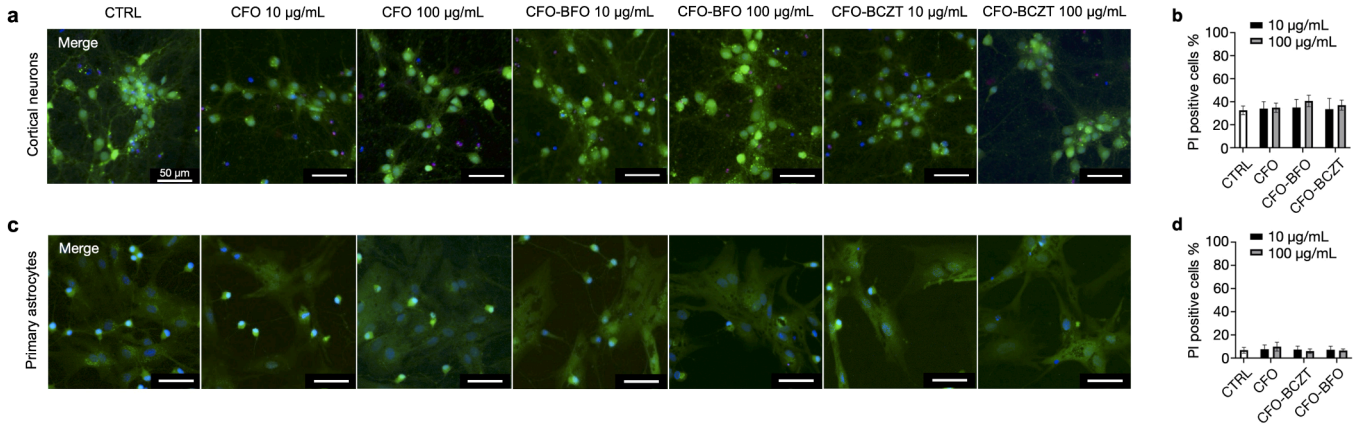

Fig. 4. The impact of CFO, CFO-BFO, and CFO-BCZT MENPs on **a-b)** primary cortical neuron and **c-d)** astrocyte viability after 24 h of incubation at low (10 µg/mL) and high (100 µg/mL) concentrations. Representative Propidium iodide (red)/Calcein (green)/Hoechst (blue) staining of **a)** cortical neurons and **c)** primary astrocytes under control conditions (CTRL; untreated cells), incubated with CFO NPs (10 µg/mL and 100 µg/mL), CFO-BFO MENPs (10 µg/mL and 100 µg/mL) and CFO-BCZT MENPs (10 µg/mL and 100 µg/mL). **b, d)** Charts represent the quantification of percentage of PI-positive **b)** neurons and **d)** astrocytes in control and treatment groups. Data are expressed as the percentage of PI-positive cells on the total number of cells and presented as mean ± standard error of the mean (SEM) (n = 3 independent experiments: 24 images per group/experiment). Tukey's test after one–way analysis of variance (ANOVA) was used for statistical analysis. No significant differences have been observed between test conditions and the control.

3.3. Impact of magnetostrictive core and ME core-shell MENPs on cell viability and neuronal cell integrity in organotypic hippocampal slice cultures

We have tested the biocompatibility of the CFO-BCZT MENPs in an ex vivo model of higher complexity – the brain slices. Once again, CFO and CFO-BFO MENPs were also tested for comparison. Cell viability upon incubation with MENPs was evaluated through PI uptake and neuronal cell integrity through β3-tubulin immunofluorescence, as previously described [35]. MENPs were applied at 7 DIV drop by drop on the top of each slice at the same concentration (400 ng/slice) and incubated for additional 14 days (Fig. 1d). Image analysis and quantification of PI uptake were carried out using image J software in the whole slice at 8, 14 and 21 DIV (Supplementary Fig. 2). At these time points, we did not observe significant differences in slices treated with the different MENPs when compared to control slices. This consistency in neuronal viability is essential, as it suggests that the MENPs do not elicit acute neurotoxic effects in a more complex tissue environment, which may differ from isolated cell cultures in vitro. In accordance with the in vitro tests conducted on primary cultures of cortical neurons, no significant differences were observed in β3-tubulin fluorescence intensity at all the three time points analyzed (Supplementary Fig. 3). In support of these findings, additional structural analysis of β3-tubulin revealed non-significant neuronal alterations in slices treated with MENPs compared to untreated cultures (Fig. 7a–c), indicating that neuronal integrity remained intact in slices treated with MENPs, which

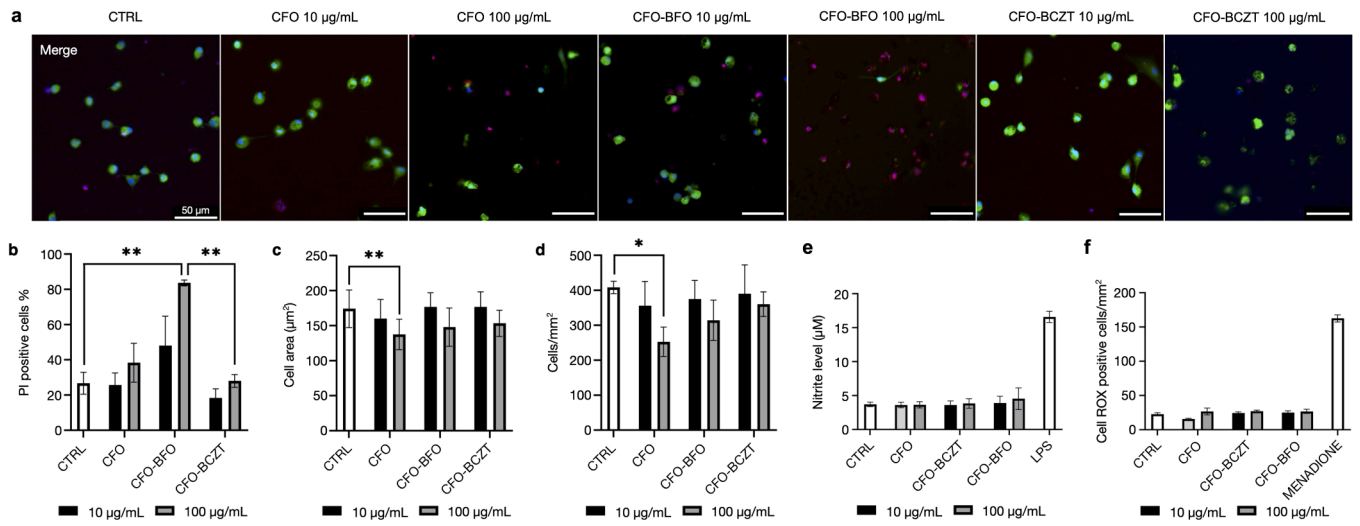

Fig. 5. The impact of CFO, CFO-BFO, and CFO-BCZT NPs on microglial cells viability after 24 h of incubation at low (10 μg/mL) and high (100 μg/mL) concentrations. **a)** Representative Propidium iodide (red)/Calcein (green)/Hoechst (blue) staining of primary microglia under control conditions (CTRL; untreated cells), incubated with CFO NPs (10 μg/mL and 100 μg/mL), CFO-BFO MENPs (10 μg/mL and 100 μg/mL), and CFO-BCZT MENPs (10 μg/mL and 100 μg/mL). **b-f)** Charts represent the quantification of **b)** percentage of PI-positive cells, **c)** cell area, **d)** cell detachment, **e)** nitrite levels, and **f)** ROS levels in control and treatment groups. Data are expressed as the percentage PI-positive cells on the total number of cells, as cell area in μm^2, as cell density in cells/mm^2, as nitrite level in μM, and as ROS level in Cell ROX positive cells/mm^2 (respectively from b to f) and presented as mean ± standard error of the mean (SEM) ($n = 3$ independent experiments: 24 images per group/experiment). Tukey's test after one–way analysis of variance (ANOVA) was used for statistical analysis. *$p < 0.05$; **$p < 0.01$.

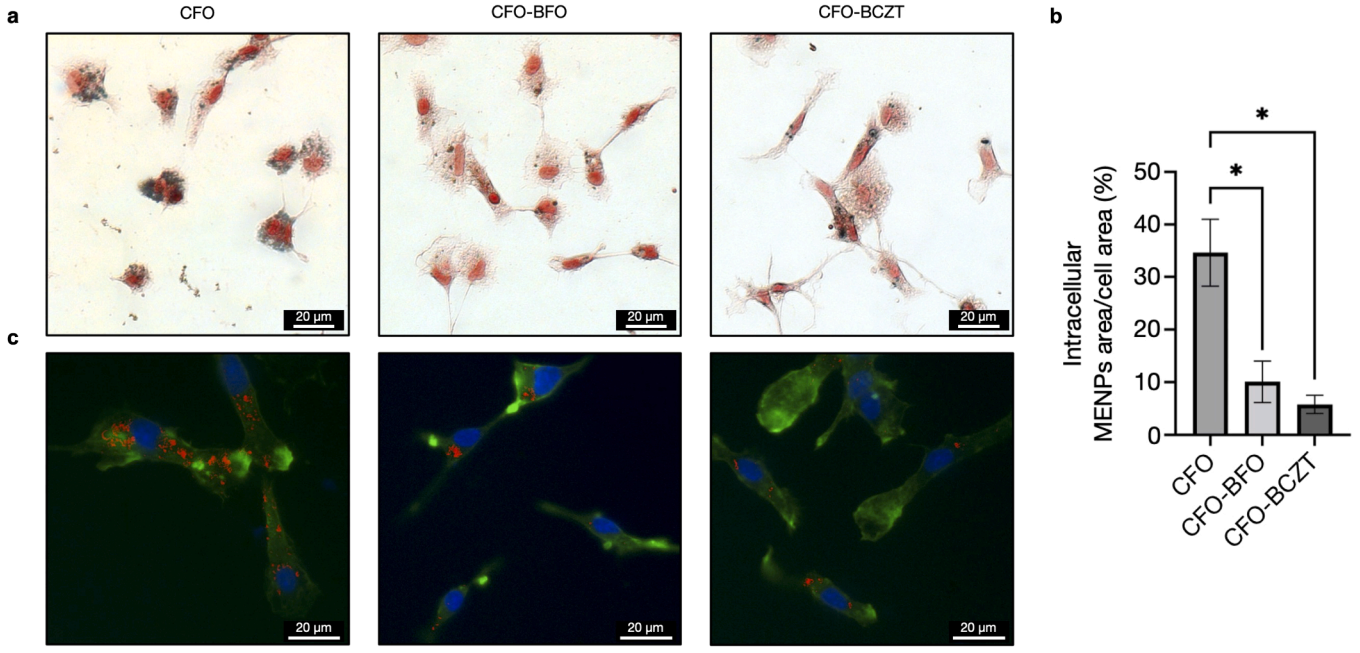

Fig. 6. The impact of CFO, CFO-BFO, and CFO-BCZT NPs on NO and ROS levels after 24 h of incubation at low (10 μg/mL) concentrations under control conditions (CTRL; untreated cells), and the internalization of NPs by microglial cells **a)** Representative fast nuclear red/Prussian blue-stained microglial cells incubated with CFO NPs (10 μg/ml), CFO-BFO MENPs (10 μg/ml) and CFO-BCZT MENPs (10 μg/ml) **b)** Chart represents NPs content in control and treatment groups. **c)** Images of Phalloidin (green)/Hoechst (blue)-stained microglia merged with brightfield showing the internalization of NPs (red). Data are expressed as the percentage of intracellular NPs area divided by the total cell area and presented as mean ± standard error of the mean (SEM) ($n = 3$ independent experiments: 24 images per group/experiment). Tukey's test after one–way analysis of variance (ANOVA) was used for statistical analysis. *$p < 0.05$.

is essential for maintaining normal synaptic function and overall neural circuit stability.

Immunofluorescence analysis on microglia and astrocytes was performed to investigate the response of glial cells to MENPs. When investigating astrocyte reactivity with GFAP immunofluorescence, we did not observe any significant increase in GFAP fluorescence intensities at all time points and treatment groups (Supplementary Fig. 4), as well as non-significant alterations in GFAP area (Fig. 7d–e). In conformity with in vitro experiments, these data indicate that astrocyte integrity remained unaltered at 21 DIV, i.e., after 14 days of contact with the examined MENPs. This absence of reactivity indicates that astrocytes maintained their integrity and did not undergo the activation typically associated with neuroinflammatory responses. This stability is promising, as astrocytes play critical roles in supporting neuronal function

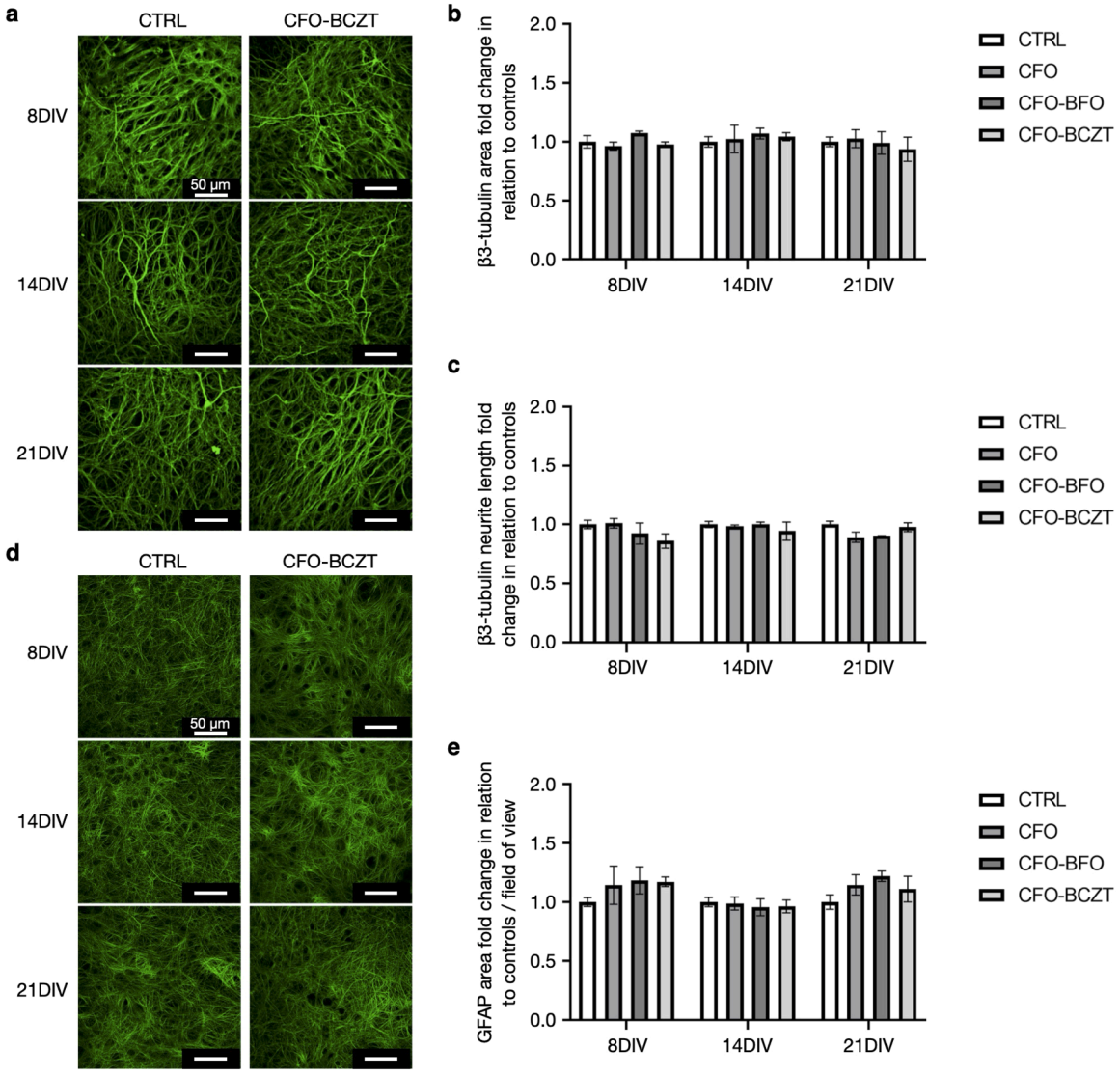

Fig. 7. The impact of CFO, CFO-BFO, and CFO-BCZT NPs on morphological alterations of β3-tubulin in organotypic hippocampal slice cultures at 8DIV, 14DIV and 21DIV (corresponding to 1 day, 7 days and 14 days in contact with the NPs). **a)** Representative β3-tubulin immunostaining of neurons under control conditions (CTRL; untreated cells) and incubated with CFO-BCZT MENPs. **b-c)** Charts represent β3-tubulin morphology quantification showing non-significant differences in **b)** the area and **c)** the total neurite length per field of view in all the treatment groups compared to controls. **d)** Representative GFAP immunostaining of organotypic hippocampal slices under control conditions (CTRL; untreated slices), and CFO-BCZT MENPs. **e)** Chart represents GFAP area quantification showing non-significant differences in GFAP area in all treatment groups compared to controls. Data are expressed as the β3-tubulin area and total β3-tubulin neurite length fold changes in relation to controls, as well as GFAP area fold change per field of view from the value of control slices and presented as mean ± standard error of the mean (SEM) (n = 3 independent experiments: 4–6 slices analyzed per group/experiment). Tukey's test after one–way analysis of variance (ANOVA) was used for statistical analysis. No significant differences have been observed between test conditions and the control.

and modulating inflammatory processes in the brain [54].

Subsequently, we performed Iba-1 fluorescence intensity measurements to investigate the impact of MENPs on microglia. Conversely to what we observed for astrocytes, our results showed a significant increase (1.3-fold) in Iba-1 fluorescence intensity in slices treated for 14 days with CFO-BFO MENPs (21 DIV), while non-significant effects were observed with uncoated CFO and CFO-BCZT MENPs (**Supplementary Fig. 5**). This is particularly noteworthy because activated microglia can influence neuronal health and contribute to neurodegenerative processes in the long term if the activation is sustained or excessive. Moreover, structural analysis of microglia morphology (Fig. 8a) showed significant alterations in slices treated with CFO and CFO-BFO MENPs. In particular, we observed significant decrease in the number of microglial branches in CFO-BFO treated slices at 14 and 21 DIV (Fig. 8b), as well as the number of endpoints (Fig. 8c), junctions (Fig. 8e) and increase in cell body areas (Fig. 8d). In line with the in vitro cell culture experiments, we observed morphological alterations also in slices treated with uncoated CFO NPs, with a significant decrease in the number of endpoints already at 14 DIV (Fig. 8c) as well as in the number of junctions at 21 DIV (Fig. 8e). Conversely, non-significant morphological alterations were observed in all the time points in slices treated with CFO-BCZT MENPs, implying that the BCZT coating displays better biocompatibility compared to uncoated CFO and CFO-BFO MENPs (Fig. 8b–c).

The contrasting responses of astrocytes and microglia to MENPs highlight the complexity of cellular interactions in the brain tissue. In both in vitro cell cultures and organotypic hippocampal slice cultures, we show that while astrocytes appear non-reactive to the presence of MENPs, microglia exhibit signs of activation after contact with MENPs, particularly in response to CFO-BFO MENPs. This differential response

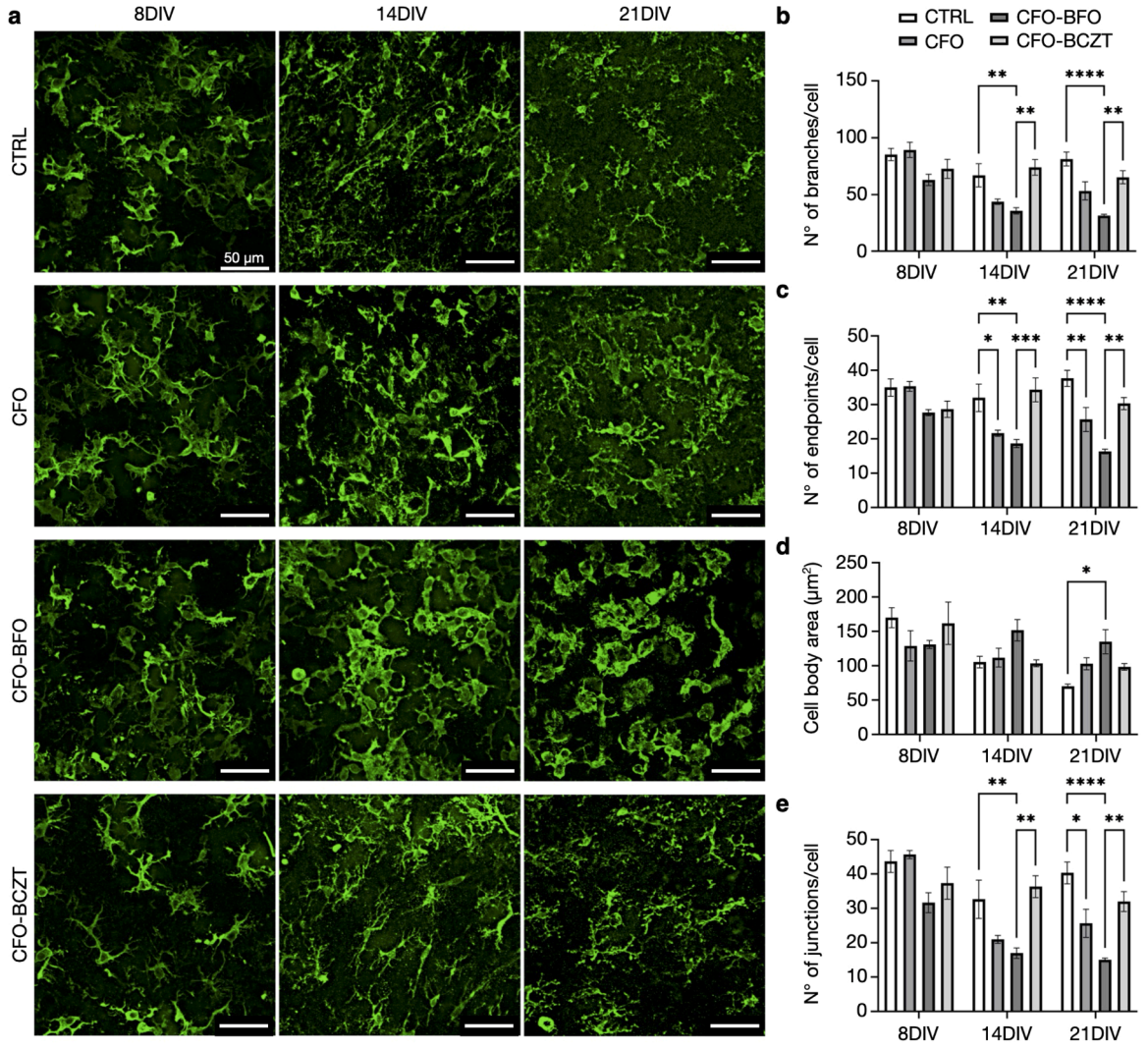

Fig. 8. The impact of CFO, CFO-BFO, and CFO-BCZT NPs on microglia activation and morphological alterations in organotypic hippocampal slice cultures at 8DIV, 14DIV and 21DIV (corresponding to 1 day, 7 days and 14 days in contact with the NPs). **a)** Representative Iba-1 staining of microglial cells under control conditions (CTRL; untreated cells), and incubated with CFO, CFO-BFO and CFO-BCZT NPs. **b-e)** Charts represent microglia morphology quantification showing **b)** the number of branches, **c)** the number of endpoints, **d)** cell body area, and **e)** number of junctions. Data are presented as means ± standard error of the mean (SEM) ($n = 3$ independent experiments; 5–8 cells analyzed per group/experiment). Tukey's test after one–way analysis of variance (ANOVA) was used for statistical analysis. *$p < 0.05$; **$p < 0.01$; ***$p < 0.001$; **** $p < 0.0009$.

could reflect the specific roles these cells play in CNS: microglia generally provide quicker responses to foreign materials in vivo, with the release of cytokines, which in turn trigger astrocytes activation, culminating in the formation of the glial scar [55,56]. However, these cellular responses may be different in terms of biochemical reactions and timing among the various biological models employed and are dependent on the physico-chemical characteristics of the materials being tested.

Overall, these findings suggest that while some NPs may be biocompatible with neurons and astrocytes, they could still generate undesirable effects in microglia that may impact brain function in the long run. This highlights the need for investigating their impact on brain tissue after prolonged exposure.

3.4. Impact of CFO-BCZT MENPs motion on brain tissue viability and integrity

The impact of CFO-BCZT MENPs motion was assessed in organotypic hippocampal slice cultures (Fig. 1e). MENPs penetration in the brain tissue imposed by the magnetic field was confirmed by the identification of CFO-BCZT MENPs in transversal cryosections of the brain slices analyzed by TEM and confocal microscopy. After staining with Prussian blue and fast nuclear red, which stain iron and nuclei, we identified the presence of CFO-BCZT MENPs deep in the brain tissue (Fig. 9a–b). The application of the magnetic plate at the bottom of the inserts for 30 min led to a penetration of around 40 µm from the top of each slice (Fig. 9c). Complementarily, confocal imaging and 3D reconstruction with the Imaris software confirmed the presence of MENPs in deep areas compared to control cultures (Fig. 9d).

Such findings were also confirmed by TEM, which also allowed for the observation of the preservation of cellular compartments such as the cytoskeleton, synapses, and mitochondria in the surroundings of MENP aggregates, regardless of their motion through the tissue (Fig. 9e–f).

To further determine the impact of motion on the brain tissue, we performed a PI assay after 24 h (Fig. 10a–b), followed by the analysis of tissue integrity by β3-tubulin immunofluorescence (Fig. 10c–e). In Fig. 10b, we show that the motion of CFO-BCZT MENPs did not hamper tissue viability 24 h post-treatment. The quantification of the number of β3-tubulin junctions (Fig. 10d) and processes' length (Fig. 10e) showed non-significant differences when comparing control slices and slices

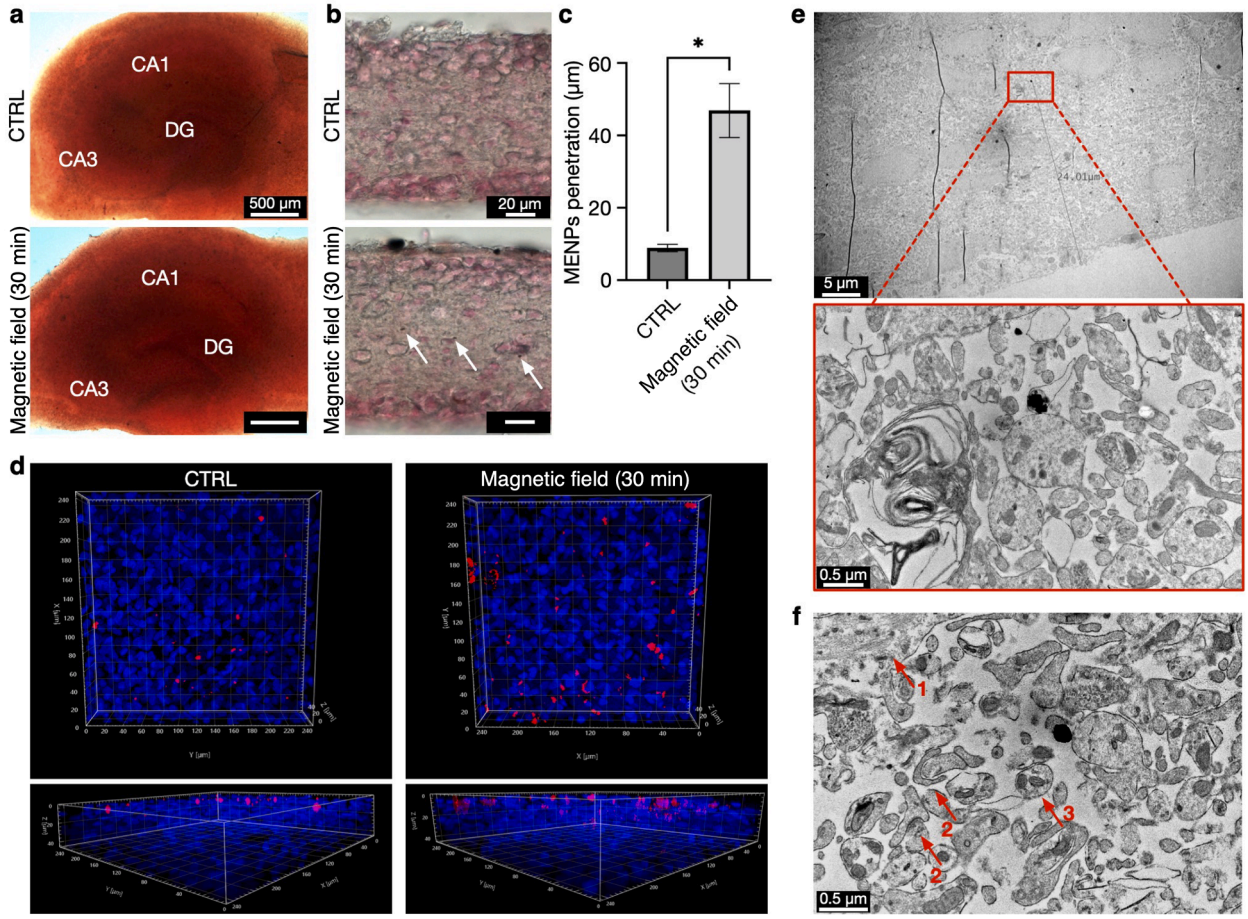

Fig. 9. CFO-BCZT MENPs penetration in the brain tissue after application of a magnetic field for 30 min using the magnetic plate. **a)** Representative Prussian blue/fast nuclear red-stained organotypic hippocampal slices under control conditions (CTRL slices treated with CFO-BCZT MENPs), and after applying magnetic field for 30 min using a magnetic plate. **b)** Images of stained 20 µm organotypic hippocampal cryosections show CFO-BCZT MENPs' penetration into the tissue. White arrows indicate CFO-BCZT MENPs. **c)** Chart represents the quantification of CFO-BCZT MENPs penetration in both groups. **d)** Representative 3D reconstruction of Hoechst-stained organotypic hippocampal slices showing CFO-BCZT MENPs (in red) penetration through the tissue. **e)** Representative TEM image showing CFO-BCZT MENPs penetration into the brain tissue. The red square represents a higher magnification ROI showing the MENPs. **f)** TEM image of brain section showing integrity of the brain tissue surrounding a CFO-BCZT MENPs aggregate. Red arrows indicating (1) cell cytoskeleton, (2) synapses, and (3) mitochondria. Data are expressed as distance of NPs from the surface of the slice in µm and presented as means ± standard error of the mean (SEM) ($n = 3$ independent experiments; 3 slices analyzed per group/experiment). Tukey's test after one–way analysis of variance (ANOVA) was used for statistical analysis. $^*p < 0.05$.

where the magnetic field was applied, indicating that the MENPs movement did not compromise neuronal integrity.

3.5. *Impact of magnetic field stimulation on the neurite outgrowth in SH-SY5Y cells*

Stimulation of the SH-SY5Y neuronal cell line was conducted to assess the impact of magnetoelectrical stimulation on neurite outgrowth. Cells were incubated with CFO-BCZT or CFO-BFO MENPs at a concentration of 10 and 100 µg/mL and placed inside the incubator under a constant magnetic field for 24 h, followed by 24 h in normal conditions. (Fig. 1f) High-throughput image analysis and quantification of β3-tubulin (Fig. 11a–c) revealed that CFO-BFO MENPs showed a better performance at higher concentrations, with an overtly increased neurite outgrowth quantified in terms of the average total neurite length (Fig. 11b) and average length of the longest neurite per field of view (Fig. 11c). A similar tendency was observed for the CFO-BCZT MENPs. However, the obtained values did not reach statistical significance. Moreover, as seen in Fig. 11, magnetic stimulation of both core-shell MENPs led to a robust neurite extension with an overall higher β3-tubulin expression throughout the cell soma and extensions. These data indicate that 24 h of magnetic field can trigger the electrical stimulation of neuronal cells.

4. Discussion

The potential of MENPs as smart nanodevices for drug delivery or neurostimulation is undisputed [19,57]. They provide a tool for neuromodulation therapies to promote tissue regeneration [58].

Evaluating the safety and biocompatibility of newly designed MENPs is paramount to enabling the application of new technologies such as DBS and promoting the clinical progress for new treatment strategies for neurological diseases.

Potential toxicity and harmful biological effects are of further concern in the context of the central nervous system, due to the very sensitive and responsive nature of these tissues. However, despite the advances in biocompatibility and promising results from recent in vivo studies, there is still a long way to go before they are applied to human patients.

In this study, we aimed at developing and evaluating the biocompatibility of CFO-BCZT MENPs as promising multiferroic core-shell MENPs for future neural applications. We have proposed BCZT because it has been reported to display elevated biocompatibility, a higher piezoelectric coefficient than barium titanate ceramics, and

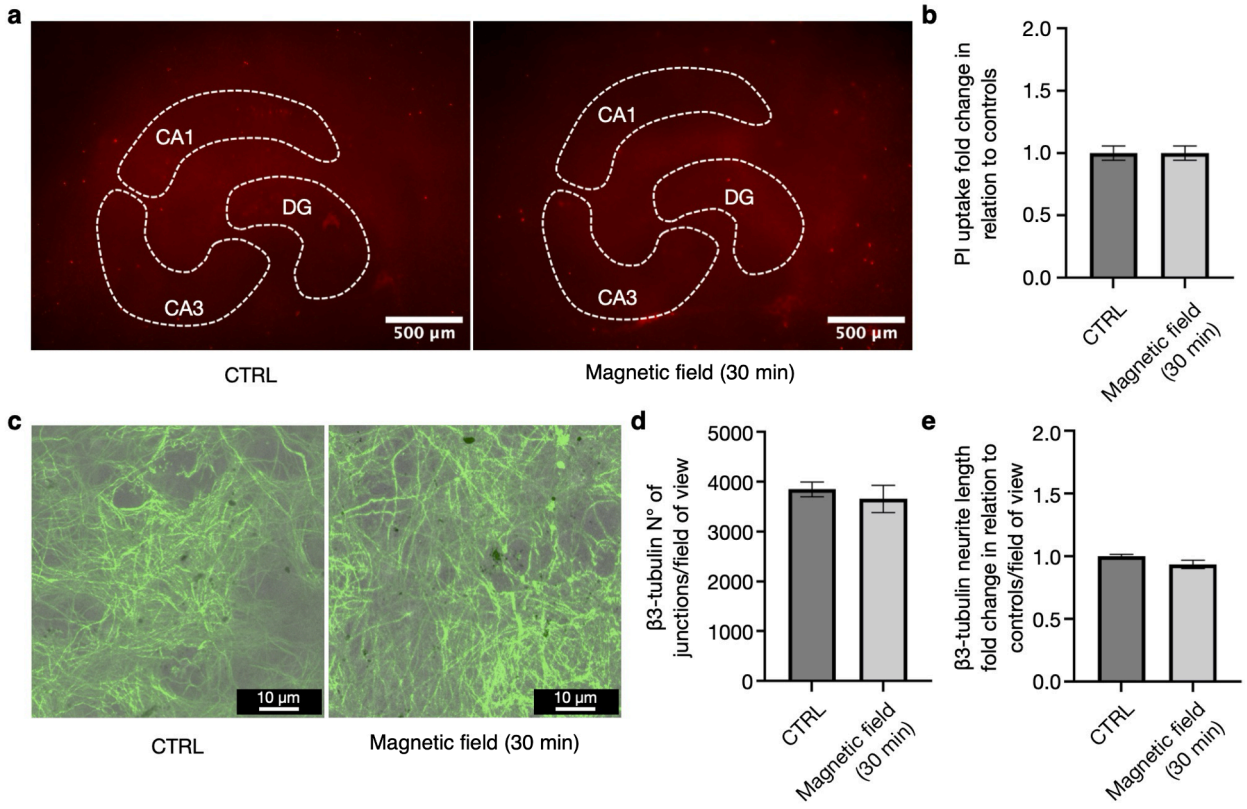

Fig. 10. The impact of CFO-BCZT MENPs penetration into the brain tissue on viability and tissue integrity after 24 h of contact. **a)** Representative PI staining of organotypic hippocampal slices after 24 h in normal conditions for control group (CTRL; slices treated with CFO-BCZT), and for the experimental group which was subjected to the magnetic field for 30 min by utilizing a magnetic plate. **b)** Chart represents the quantitative analysis of PI fluorescence intensity after 24 h. **c)** Representative β3-tubuline-stained organotypic hippocampal slices merged with brightfield showing that CFO-BCZT MENPs penetration does not hamper tissue integrity after 24 h. d-**e)** Charts represent the quantifications of **d)** the number of β3-tubulin junctions and **e)** the total β3-tubulin neurite length fold change. Data are expressed as distance of NPs from the surface of the slice in µm, number of β3-tubulin junctions per field, and total β3-tubulin neurite length fold change per field from the value of control slice and presented as means ± standard error of the mean (SEM) ($n = 3$ independent experiments; 3 slices analyzed per group/experiment). Tukey's test after one–way analysis of variance (ANOVA) was used for statistical analysis. No significant differences have been observed between test conditions and the control.

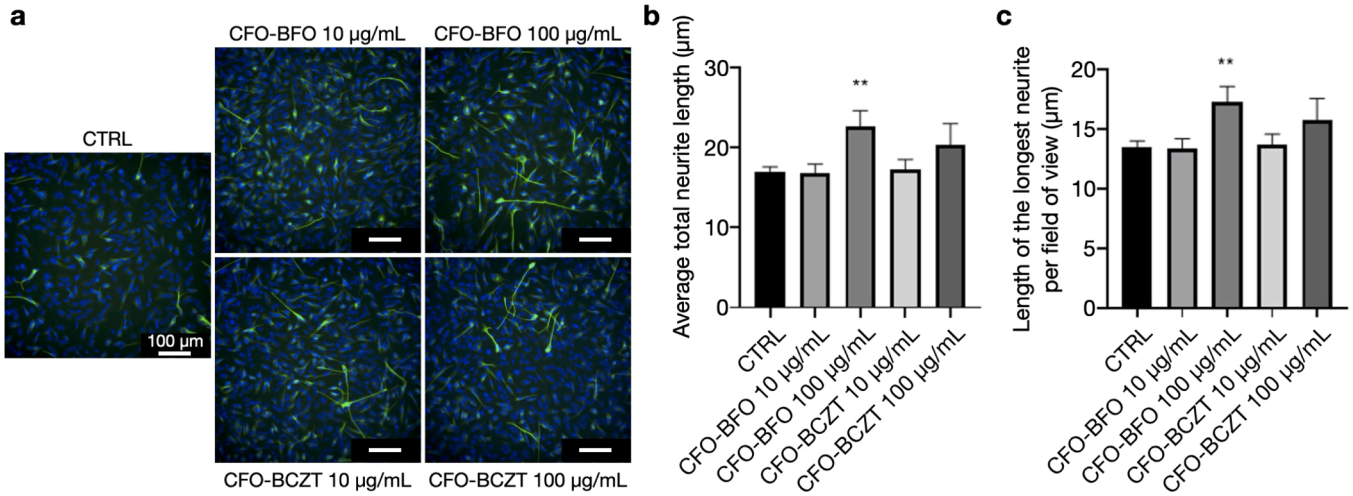

Fig. 11. Effect of 24 h magnetic stimulation with MENPs on neurite outgrowth in SH-SY5Y cells. CFO-BFO and CFO-BCZT MENPs were tested at both low (10 µg/mL) and high (100 µg/mL) concentrations compared to the control group (CTRL) **a)** Fluorescent images are representative of β3-tubulin (green) and Hoechst (blue) staining of SH-SY5Y cells under control conditions (CTRL), as well as incubated with CFO-BFO and CFO-BCZT MENPs at a concentration of both 10 and 100 µg/ml. White arrows highlight the longest neurite. **b-c)** Charts represent the quantifications of **b)** the average total β3-tubulin neurite length per field of view, and **c)** the length of the longest neurite per field of view, all normalized for cell density. Four independent experiments with technical triplicates were performed and analyzed. Data are expressed in µm and presented as mean ± STDEV (75 images analyzed per group) of one set of experiments in triplicates. Tukey's multiple comparison test after two–way ANOVA was used for statistical analysis. $^{**}p < 0.01$.

proven suitability for neurosciences [28,29,59].

We have successfully synthesized functional multiferroic core-shell cobalt ferrite (CFO) NPs coated with calcium/zirconium-doped barium titanate (CFO-BCZT) and bismuth ferrite (CFO-BFO) as a reference coating with hydrothermal and sol-gel processes. X-ray diffraction studies confirmed the cubic Fd-3 m space group of CFO core NPs, the hexagonal R3c BFO shell, and the tetragonal P4mm BCZT shell. HAADF-STEM and EDX images confirmed the core-shell structure of both CFO-BFO and CFO-BCZT MENPs, a size of 35 ± 8 nm of CFO core, the thickness of BFO shell around 2 ± 1 nm, and thin and thick BCZT shells around 2 ± 1 nm and 15 ± 5 nm, respectively. PFM has shown that both MENPs display the magnetoelectric coupling effect. Subsequently, we evaluated their biocompatibility in vitro and ex vivo. For in vitro studies, concentrations of 10 and 100 μg/mL were selected because they align with commonly used dose ranges in the literature for assessing biocompatibility. For example, in vitro studies using neuronal cell cultures have employed similar concentrations of NPs in viability, metabolic, and morphological assays [60,61]. Other studies involving MENPs have used comparable or even higher concentrations [19,62–64]. In our case, the two concentrations (10 and 100 μg/mL) were also chosen to provide a low and high exposure range, enabling detection of potential dose-dependent effects concerning the analytical methods employed. A total dose of 400 ng of NPs per slice was selected for organotypic hippocampal slice cultures to reflect a high dose for prolonged exposure in vivo. The dosing strategy that we have performed was established in our recent study [35] in which we applied the NPs directly onto the top surface of each brain slice. This approach differs from that used in traditional in vitro 2D cell cultures and short-term ex vivo organotypic cultures, where NPs concentrations typically are in the μg/mL range in the culture medium [65–67], and from in vivo studies where administered doses can vary from μg to mg depending on the administration route, reaching approximately μg-level total brain accumulation [11, 68–70]. This direct application method offers several advantages, as it ensures adequate interaction of the NPs with the tissue and maximizes both uniform exposure and effective tissue-material contact across the entire slice. In addition, preliminary titration experiments were conducted to identify the optimal dose that provided sufficient NP accumulation within the tissue to support all planned analyses, including cellular response studies, imaging, and quantification assays.

With our in vitro studies, employing primary cortical neurons, microglia, and astrocytes, we reported that the CFO-BCZT MENPs displayed better biocompatibility over CFO-BFO MENPs and uncoated CFO NPs at high concentrations, with the former having no significant impact on neural cell viability and glial cell activation. While we showed that all tested MENPs did not cause significant cell death in primary cultures of astrocytes and cortical neurons, at the two tested concentrations, the NPs' behavior was different when in contact with microglia. For these cells, we observed that the treatment for 24 h with CFO-BFO MENPs at the highest concentration caused a significant impairment in microglial cell viability compared to controls. Interestingly, such effects were not associated with increased NO and ROS production or with MENPs internalization. The internalization studies showed that uncoated CFO NPs are more internalized than CFO-BCZT and CFO-BFO MENPs, as both coatings make the microglia less prone to phagocytic activity. However, BFO coating caused significant impairment in microglial viability at high concentrations regardless of ROS and NO production. This can be explained by electrostatic interactions between the NPs and the cell membranes [25]. For the CFO NPs, we observed microglial shrinkage and detachment at high concentrations after 24 h of treatment due to CFO's enhanced cell engulfment and intrinsic toxicity. Such toxicity may be mitigated by the presence of the BCZT shell, possibly due to the reduction in the cobalt ions leaching out from the CFO core [71].

The brain tissue response was evaluated in the ex vivo rat organotypic hippocampal slice cultures, focusing on the CA1, CA3, and DG subregions, as the most susceptible to cellular responses. Our results, which are commensurate with the in vitro studies, showed that, while non-significant effects were observed in neurons and astrocytes, Iba-1 fluorescence intensity was increased in slices treated with CFO-BFO MENPs at 21 DIV compared to uncoated CFO NPs, CFO-BCZT MENPs, and control cultures, as a result of microglia activation upon material contact. Moreover, the microglia morphology analysis revealed significant alterations from 14 DIV in slices treated with uncoated CFO and, to a greater extent, with CFO-BFO MENPs. Interestingly, no adverse effects were observed with CFO-BCZT MENPs at all the time points investigated.

Our results on BFO effects at high concentrations follow other recent in vitro studies investigating bismuth-based materials' toxic effects. Song and co-workers reported dose-dependent neurotoxicity in PC12 pheochromocytoma rat cell lines exposed to high BFO NPs. Such effects were mainly caused by the interaction of BFO NPs with the cell membranes, resulting in decreased cell adhesion and proliferation [23]. Gao and colleagues reported a dose-dependent reduction in viability in human skin-derived cell lines treated with bismuth oxybromide NPs, namely damaging cell membrane integrity and induction of apoptosis [24]. Similarly, Staedler and colleagues reported moderate cytotoxicity of human adenocarcinoma (A549), lung squamous carcinoma (NCI-H520), and, to a greater extent, acute monocytic leukemia (THP-1) cell lines exposed to BFO NPs for 72 h. Interestingly, such cytotoxicity was less pronounced when the NPs were coated with polyethylene glycol, suggesting that BFO NPs interfere with the physiology of the cell membrane [25]. Moreover, several clinical studies reported cases of bismuth intoxication in patients undergoing prolonged exposure to high levels of bismuth-based drugs [72,73]. Two cases of bismuth neurotoxicity were reported in patients undergoing treatment with bismuth iodoform paraffin paste as an antiseptic after surgical operation in the jaws. The patients presented confusion, high levels of bismuth concentration in the blood, and one of them also experienced depression and suicidal thoughts [74]. Borbinha and colleagues described a case of bismuth neurotoxicity in a patient undergoing bismuth subsalicylate supplementation for several years to treat gastrointestinal complaints. The patient presented abnormal behavior, confusion, encephalopathy, and myoclonus, accompanied by high levels of bismuth in urine, serum, and cerebrospinal fluid [27]. Similar neurotoxic effects have been described in a woman after chronic ingestion of bismuth subgallate to treat gastrointestinal symptoms. This patient presented progressive encephalopathy, aphasia, myoclonus, and gait instability [26]. These observations indicate that, although multiple in vitro and clinical studies reported potential toxic effects associated with BFO exposure, its overall safety in humans remains uncertain, as these responses are complex and may be context dependent. Our findings demonstrating BFO-induced cytotoxicity in microglial cells, combined with current knowledge, highlight the need for further investigations to elucidate the mechanisms underlying BFO neurotoxic potential.

Here, further studies on the impact of MENPs' motion through the brain tissue were carried out in organotypic hippocampal slice cultures with CFO-BCZT MENPs. We progressed with the experiments only with CFO-BCZT MENPs due to their superior biological performance and because the magnetic attraction effect would mainly depend on the CFO core, regardless of the shell type. We successfully induced CFO-BCZT MENPs motion through the tissue using a magnetic plate placed on the bottom of the well plate for 30 min. Additionally, we showed that such penetration from the top of the slices inwards was harmless and did not cause any effects on the integrity of tissue architecture or cell death after 24 h. Due to the lack of such studies in the literature, we showed throughout this work the versatility of organotypic cultures as an advanced platform to investigate the effects of motion of the various core-shell MENPs developed, as they offer the possibility to dissect their impact at the cellular level over extended periods of time in a living 3D tissue that closely mimics the in vivo scenario.

Preliminary in vitro experiments on stimulation of the human neuronal SH-SY5Y cells were carried out with CFO-BCZT and CFO-BFO MENPs at 10 and 100 μg/mL. This is an ideal range of concentration

known to elicit neuronal response upon electrical stimulation, taking into consideration previously reported in vitro studies [75–77]. Our results indicate that both types of MENPs led to notable neurite extension under magnetic stimulation. CFO-BFO MENPs exhibited superior performance at higher concentrations in terms of the average total and longest neurite length. This suggests that the CFO-BFO MENPs may provide a potent means of inducing neuronal outgrowth through magnetoelectric stimulation.

However, when considering the results of the previous biocompatibility studies, the CFO-BFO MENPs raise concerns regarding their safety, particularly their effects on glial cell viability and microglial activation. These MENPs showed toxicity at elevated concentrations in primary cultures of microglia and in organotypic hippocampal slices. This is a critical limitation when considering follow-up studies with animal models. In contrast, the CFO-BCZT MENPs exhibited better overall biocompatibility while demonstrating slightly less pronounced ability to promote neurite outgrowth than CFO-BFO. As highlighted in our biocompatibility assays, CFO-BCZT MENPs showed minimal toxicity at high concentrations, with no significant adverse effects on neural cell viability, microglial activation, or astrocyte function. These data indicate that CFO-BCZT MENPs are well tolerated in biological systems. This provides a safe and robust starting point for future studies to identify the minimum effective concentration required to achieve the desired biological outcomes. Further optimizations can be pursued both at the material level, such as adjustments in size, shape, and core-shell structure to enhance magnetoelectric properties, and in the parameters of the external magnetic field, such as intensity, frequency, and exposure duration, to ameliorate the overall efficiency of the biological response and safety in future therapeutic applications.

The results presented herein suggest that CFO-BCZT MENPs represent a safer alternative for wireless and non-invasive neuronal stimulation and may offer better perspectives for in vivo applications, where long-term safety and biocompatibility are paramount. Although not investigated, such effects could be explained by the generation of action potentials by membrane depolarization, enhanced expression of neuron-specific proteins, neurotrophic factors release, and enhancement of autophagy signaling in response to the localized electric fields at the nanoscale level produced by MENPs under magnetic stimulation [77–79]. Future work will explore the mechanisms and features of our MENPs and their impact on neuronal excitability and connectivity under magnetic stimulation. These are relevant for further developments of this class of MENPs and their application in wireless and non-invasive neuronal stimulation approaches to restore the neurological functions of damaged tissues.

In conclusion, here we demonstrated the ability of the proposed BCZT coating to confer magnetoelectric coupling effect to CFO NPs and to sustain better biocompatibility compared to BFO in vitro and ex vivo. We also showed the capability of CFO-BCZT MENPs to be guided through the brain by external magnetic field application safely without compromising tissue viability and neuronal integrity, and to evoke wireless neuronal electrical stimulation that promotes neurite outgrowth. In light of these observations, our findings confirm the favorable potential of BCZT for the design of biocompatible multiferroic core-shell MENPs for applications in the central nervous tissue. Further, these indicate that the proposed approach can lead the field toward the direction of the successful translation of MENPs for the treatment of diverse neurological conditions.

CRediT authorship contribution statement

Maurizio Gulino: Writing – review & editing, Writing – original draft, Visualization, Investigation, Data curation. **Donghoon Kim:** Writing – review & editing, Writing – original draft, Investigation, Data curation. **Qiao Tang:** Writing – review & editing, Data curation. **Semih Sevim:** Writing – review & editing, Visualization. **Elric Zhang:** Writing – review & editing. **Hao Ye:** Writing – review & editing. **Xiang-Zhong Chen:** Writing – review & editing, Supervision, Data curation. **Miguel Rafael Gonçalves Morais:** Visualization, Investigation, Data curation. **Sofia Duque Santos:** Writing – review & editing, Supervision, Methodology, Investigation, Data curation, Conceptualization. **Salvador Pané:** Writing – review & editing, Supervision, Funding acquisition, Data curation, Conceptualization. **Ana Paula Pêgo:** Writing – review & editing, Supervision, Project administration, Methodology, Investigation, Funding acquisition, Conceptualization.

Declaration of competing interest

The authors declare that they have no known competing financial interests or personal relationships that could have appeared to influence the work reported in this paper.

Acknowledgements

This project was funded by the European Union's Horizon 2020 Research and Innovation Programme under the Marie Skłodowska-Curie grant agreement No. 764977, in the framework of the mCBEEs project (Advanced integrative solutions to corrosion problems beyond microscale: toward long-term durability of miniaturized biomedical, electronic, and energy systems). The authors thank the support of the i3S Scientific Platforms Bioimaging, Advanced Light Microscopy (ALM), Histology and Electron Microscopy (HEMS), members of the national infrastructure PPBI–Portuguese Platform of Bioimaging (PPBI-POCI-01-0145-FEDER-022122), and the BioSciences Screening, member of the PT-OPENSCREEN (NORTE-01-0145-FEDER-085468) and PPBI (PPBI-POCI-01-0145-FEDER-022122). The authors acknowledge Enric Menendez from the Autonomous University of Barcelona for his assistance with the Rietveld refinement. The authors would also like to thank the Scientific Center for Optical and Electron Microscopy (ScopeM), and the FIRST laboratory at ETH for their technical support. APP acknowledges the MOBILIsE Project, which has received funding from the European Union's Horizon 2020 research and innovation program under grant agreement no.951723. SS and MRGM acknowledge FCT for the contract under the Norma Transitória (DL57/2016/CP/CP1360/CT0013) and the PhD scholarship (2022.13353.BD), respectively. SP acknowledges the funding from the European Research Council Consolidator Grant "Highly Integrated Nanoscale Robots for Targeted Delivery to the Central Nervous System" (HINBOTS) under the grant no. 771565, and the Swiss State Secretariat for Education, research and Innovation (SERI) in the frame of the European Union's Horizon Europe Research and Innovation Programme (HORIZON-EIC-2021-PATHFINDEROPEN-01) under EVA project (GA No: 101047081), and the European Union's Horizon Europe Research and Innovation Programme (HORIZON-EIC-2023-PATHFINDEROPEN-01) under META-BRAIN project (GA No. 101130650).

Supplementary materials

Supplementary material associated with this article can be found, in the online version, at doi:10.1016/j.actbio.2025.11.038.

References

[1] N. Attal, F. Poindessous-Jazat, E. De Chauvigny, C. Quesada, A. Mhalla, S. S. Ayache, C. Fermanian, J. Nizard, R. Peyron, J.-P. Lefaucheur, D. Bouhassira, Repetitive transcranial magnetic stimulation for neuropathic pain: a randomized multicentre sham-controlled trial, Brain 144 (2021) 3328–3339.
[2] P.B. Fitzgerald, Targeting repetitive transcranial magnetic stimulation in depression: do we really know what we are stimulating and how best to do it? Brain Stimul. 14 (2021) 730–736.
[3] Z.-D. Deng, S.H. Lisanby, A.V. Peterchev, Coil design considerations for deep transcranial magnetic stimulation, Clin. Neurophysiol. 125 (2014) 1202–1212.
[4] S. Kopyl, R. Surmenev, M. Surmeneva, Y. Fetisov, A. Kholkin, Magnetoelectric effect: principles and applications in biology and medicine– a review, Mater. Today Bio. 12 (2021) 100149.

[5] X.-Z. Chen, J.-H. Liu, M. Dong, L. Müller, G. Chatzipirpiridis, C. Hu, A. Terzopoulou, H. Torlakcik, X. Wang, F. Mushtaq, J. Puigmartí-Luis, Q.-D. Shen, B.J. Nelson, S. Pané, Magnetically driven piezoelectric soft microswimmers for neuron-like cell delivery and neuronal differentiation, Mater. Horiz. (2019) 1512–1516.
[6] T.S. Stewart, A. Nagesetti, R. Guduru, P. Liang, E. Stimphil, A. Hadjikhani, L. Salgueiro, J. Horstmyer, R. Cai, A. Schally, S. Khizroev, Magnetoelectric nanoparticles for delivery of antitumor peptides into glioblastoma cells by magnetic fields, Nanomedicine 13 (2018) 423–438.
[7] K. Shahzad, S. Mushtaq, M. Rizwan, W. Khalid, M. Atif, F.U. Din, N. Ahmad, R. Abbasi, Z. Ali, Field-controlled magnetoelectric core-shell CoFe2O4@BaTiO3 nanoparticles as effective drug carriers and drug release in vitro, Mater. Sci. Eng.: C 119 (2021) 111444.
[8] A. Kaushik, J. Rodriguez, D. Rothen, V. Bhardwaj, R.D. Jayant, P. Pattany, B. Fuentes, H. Chand, N. Kolishetti, N. El-Hage, K. Khalili, N.S. Kenyon, M. Nair, MRI-guided, noninvasive delivery of magneto-electric drug nanocarriers to the brain in a nonhuman primate, ACS Appl. Bio Mater. 2 (2019) 4826–4836.
[9] M. Pardo, E.R. Roberts, K. Pimentel, Y.A. Yildirim, B. Navarrete, P. Wang, E. Zhang, P. Liang, S. Khizroev, Size-dependent intranasal administration of magnetoelectric nanoparticles for targeted brain localization, Nanomedicine 32 (2021) 102337.
[10] A. Jahanshahi, K. Kozielski, Y. Temel, M. Sitti, Wireless deep brain stimulation in freely moving mice with nonresonant powering of magnetoelectric nanoparticles, Brain Stimul.: Basic Transl. Clin. Res. Neuromodulation 14 (2021) 1742.
[11] T. Nguyen, J. Gao, P. Wang, A. Nagesetti, P. Andrews, S. Masood, Z. Vriesman, P. Liang, S. Khizroev, X. Jin, Vivo wireless brain stimulation via non-invasive and targeted delivery of magnetoelectric nanoparticles, Neurotherapeutics 18 (2021) 2091–2106.
[12] L. Signorelli, A. Wolters, V.Durán Toro, J. Englhard, M.S. Baghini, E. Koçar, F. Wasner, N.I. Goldenstein, H. Heidari, J. Bachmann, S. Hescham, D. Gregurec, Biocompatible PVDF nanofibers with embedded magnetite nanodiscs enable wireless magnetoelectric stimulation in premotor cortex, Adv. Heal. Mater (2025) e03082.
[13] Y. Zhang, S. Chen, Z. Xiao, X. Liu, C. Wu, K. Wu, A. Liu, D. Wei, J. Sun, L. Zhou, H. Fan, Magnetoelectric nanoparticles Incorporated biomimetic matrix for wireless electrical stimulation and nerve regeneration, Adv. Heal. Mater. 10 (2021) 2100695.
[14] R.V. Chernozem, A.O. Urakova, P.V. Chernozem, D.A. Koptsev, Y.R. Mukhortova, I. Yu. Grubova, D.V. Wagner, E.Yu. Gerasimov, M.A. Surmeneva, A.L. Kholkin, R. A. Surmenev, Novel biocompatible magnetoelectric MnFe2O4 core@BCZT shell nano–Hetero-structures with efficient catalytic performance, Small 19 (2023) 2302808.
[15] V. Herynek, L. Rajsiglová, M. Babič, M. Švábová, J. Kohout, M. Veverka, T. Kmječ, L. Kubíčková, J. Karela, F. Gregar, M. Loula, S. Matějková, L. Šefc, L. Vannucci, Nickel ferrite nanoparticles for In vivo multimodal magnetic resonance and magnetic particle imaging, ACS Appl. Nano Mater. 8 (2025) 14867–14881.
[16] P. Kumari, H. Wunderlich, A. Milojkovic, J.E. López, A. Fossati, A. Jahanshahi, K. Kozielski, Multiscale modeling of magnetoelectric nanoparticles for the analysis of spatially selective neural stimulation, Adv. Heal. Mater 13 (2024) 2302871.
[17] E. Zhang, M. Shotbolt, C.-Y. Chang, A. Scott-Vandeusen, S. Chen, P. Liang, D. Radu, S. Khizroev, Controlling action potentials with magnetoelectric nanoparticles, Brain Stimul. 17 (2024) 1005–1017.
[18] L. Wang, P. Dang, H. Zheng, L. Wei, S. Jiang, J. Wang, Y. Cai, W. Wang, C. Zhang, N. Li, J. Xia, AC magnetic field-driven wireless charging dual-oriented fibrous magnetoelectric scaffold CFO/PVDF promotes peripheral nerve repair, Colloids Surf. Physicochem. Eng. Asp. 701 (2024) 134822.
[19] R. Guduru, P. Liang, J. Hong, A. Rodzinski, A. Hadjikhani, J. Horstmyer, E. Levister, S. Khizroev, Magnetoelectric 'spin'on stimulating the brain, Nanomedicine 10 (2015) 2051–2061.
[20] Y.J. Kim, N. Kent, E. Vargas Paniagua, N. Driscoll, A. Tabet, F. Koehler, E. Malkin, E. Frey, M. Manthey, A. Sahasrabudhe, T.M. Cannon, K. Nagao, D. Mankus, M. Bisher, G. de Nola, A. Lytton-Jean, L. Signorelli, D. Gregurec, P. Anikeeva, Magnetoelectric nanodiscs enable wireless transgene-free neuromodulation, Nat. Nanotechnol. 20 (2025) 121–131.
[21] M. Dong, X. Wang, X. Chen, F. Mushtaq, S. Deng, C. Zhu, H. Torlakcik, A. Terzopoulou, X. Qin, X. Xiao, 3D-printed soft magnetoelectric microswimmers for delivery and differentiation of neuron-like cells, Adv. Funct. Mater. 30 (2020) 1910323.
[22] F. Mushtaq, H. Torlakcik, Q. Vallmajo-Martin, E.C. Siringil, J. Zhang, C. Röhrig, Y. Shen, Y. Yu, X.-Z. Chen, R. Müller, Magnetoelectric 3D scaffolds for enhanced bone cell proliferation, Appl. Mater. Today 16 (2019) 290–300.
[23] Q. Song, Y. Liu, Z. Jiang, M. Tang, N. Li, F. Wei, G. Cheng, The acute cytotoxicity of bismuth ferrite nanoparticles on PC12 cells, J. Nanoparticle Res. 16 (2014) 2408.
[24] X. Gao, Y. Wang, S. Peng, B. Yue, C. Fan, W. Chen, X. Li, Comparative toxicities of bismuth oxybromide and titanium dioxide exposure on human skin keratinocyte cells, Chemosphere 135 (2015) 83–93.
[25] D. Staedler, S. Passemard, T. Magouroux, A. Rogov, C.M. Maguire, B.M. Mohamed, S. Schwung, D. Rytz, T. Jüstel, S. Hwu, Y. Mugnier, R. Le Dantec, Y. Volkov, S. Gerber-Lemaire, A. Prina-Mello, L. Bonacina, J.-P. Wolf, Cellular uptake and biocompatibility of bismuth ferrite harmonic advanced nanoparticles, Nanomedicine 11 (2015) 815–824.
[26] P.J. Sampognaro, K.T. Vo, M.B. Richie, P.D. Blanc, K.J. Keenan, Bismuth subgallate toxicity in the age of online supplement use, Neurologist 22 (2017) 237–240.
[27] C. Borbinha, F. Serrazina, M. Salavisa, M. Viana-Baptista, Bismuth encephalopathy-a rare complication of long-standing use of bismuth subsalicylate, BMC. Neurol. 19 (2019) 212.
[28] N.D. Scarisoreanu, F. Craciun, V. Ion, R. Birjega, A. Bercea, V. Dinca, M. Dinescu, L. E. Sima, M. Icriverzi, A. Roseanu, L. Gruionu, G. Gruionu, Lead-free piezoelectric (Ba,Ca)(Zr,Ti)O3 thin films for biocompatible and flexible devices, ACS. Appl. Mater. Interfaces. 9 (2017) 266–278.
[29] K.K. Poon, M.C. Wurm, D.M. Evans, M.-A. Einarsrud, R. Lutz, J. Glaum, Biocompatibility of (Ba,Ca)(Zr,Ti)O3 piezoelectric ceramics for bone replacement materials, J. Biomed. Mater. Res. B Appl. Biomater. 108 (2020) 1295–1303.
[30] M. Wu, R. Yao, C. Jin, Y. Xu, J. Xu, L. He, Y. Yang, Y. Liu, L. Zhong, J. Gao, Significantly enhanced piezoelectric properties of BaTiO3-based ceramics with unchanged curie temperature via local chemical inhomogeneity, Chem. Eng. J. 518 (2025) 164844.
[31] S. Merselmiz, Z. Hanani, D. Mezzane, A.G. Razumnaya, M. Amjoud, L. Hajji, S. Terenchuk, B. Rožič, I.A. Luk'yanchuk, Z. Kutnjak, Thermal-stability of the enhanced piezoelectric, energy storage and electrocaloric properties of a lead-free BCZT ceramic, RSC Adv. 11 (2021) 9459.
[32] A.S. Kumar, C.S.C. Lekha, S. Vivek, V. Saravanan, K. Nandakumar, S.S. Nair, Multiferroic and magnetoelectric properties of Ba0.85Ca0.15Zr0.1Ti0.9O3–CoFe2O4 core–shell nanocomposite, J. Magn. Magn. Mater. 418 (2016) 294–299.
[33] P. Praveen, V. Monaji, E. Chandrakala, S. Indla, D. Kumar, S. V, D. Das, Enhanced magnetoelectric coupling in Ti and Ce substituted lead free CFO-BCZT laminate composites, J. Alloys. Compd. 750 (2018) 392–400.
[34] C. Li, J. Zhang, Y. Yuan, H. Zhang, X. Yan, Q. Zhao, Y. Lin, A simple and low-cost method of preparing CoFe2O4/Ba0.85Ca0.15Zr0.1Ti0.9O3 composite ceramics, J. Mater. Sci.: Mater. Electron. 33 (2022) 3757–3773.
[35] M. Gulino, S.D. Santos, A.P. Pêgo, Biocompatibility of platinum nanoparticles in brain ex vivo models in physiological and pathological conditions, Front. Neurosci. 15 (2021) 787518.
[36] M. Gulino, D. Kim, S. Pané, S.D. Santos, A.P. Pêgo, Tissue response to neural implants: the use of model systems toward new design solutions of implantable microelectrodes, Front. Neurosci. 13 (2019) 689.
[37] X. Opitz-Araya, A. Barria, Organotypic hippocampal slice cultures, J. Vis. Exp. (2011) 2462.
[38] B. Ramaswamy, S.D. Kulkarni, P.S. Villar, R.S. Smith, C. Eberly, R.C. Araneda, D. A. Depireux, B. Shapiro, Movement of magnetic nanoparticles in brain tissue: mechanisms and impact on normal neuronal function, Nanomedicine 11 (2015) 1821–1829.
[39] E. Kim, S. Jeon, Y.-S. Yang, C. Jin, J. Kim, Y.-S. Oh, J.-C. Rah, H. Choi, A neurospheroid-based microrobot for targeted neural connections in a hippocampal slice, Adv. Mater. 35 (2023) 2208747.
[40] F. Mushtaq, X. Chen, H. Torlakcik, C. Steuer, M. Hoop, E.C. Siringil, X. Marti, G. Limburg, P. Stipp, B.J. Nelson, S. Pané, Magnetoelectrically driven catalytic degradation of organics, Adv. Mater. 31 (2019) 1901378.
[41] D. Kim, I. Efe, H. Torlakcik, A. Terzopoulou, A. Veciana, E. Siringil, F. Mushtaq, C. Franco, D. von Arx, S. Sevim, J. Puigmartí-Luis, B. Nelson, N.A. Spaldin, C. Gattinoni, X.-Z. Chen, S. Pané, Magnetoelectric effect in hydrogen harvesting: magnetic field as a trigger of catalytic reactions, Adv. Mater. 34 (2022) 2110612.
[42] K.D. McCarthy, J. de Vellis, Preparation of separate astroglial and oligodendroglial cell cultures from rat cerebral tissue, J. Cell Biol. 85 (1980) 890–902.
[43] D.N. Rocha, E.D. Carvalho, L.R. Pires, C. Gardin, I. Zanolla, P.K. Szewczyk, C. Machado, R. Fernandes, U. Stachewicz, B. Zavan, J.B. Relvas, A.P. Pêgo, It takes two to remyelinate: a bioengineered platform to study astrocyte-oligodendrocyte crosstalk and potential therapeutic targets in remyelination, Biomater. Adv. 151 (2023) 213429.
[44] L.G.W. Hilgenberg, M.A. Smith, Preparation of dissociated mouse cortical neuron cultures, J. Vis. Exp. (2007) 562.
[45] N. Cho, E.H. Moon, H.W. Kim, J. Hong, J.A. Beutler, S.H. Sung, Inhibition of nitric oxide production in BV2 microglial cells by triterpenes from Tetrapanax papyriferus, Molecules. 21 (4) (2016) 459, 21.
[46] J. Neubert, S. Wagner, J. Kiwit, A.U. Bräuer, J. Glumm, New findings about iron oxide nanoparticles and their different effects on murine primary brain cells, Int. J. Nanomed. 10 (2015) 2033–2049.
[47] H. Hojo, K. Oka, K. Shimizu, H. Yamamoto, R. Kawabe, M. Azuma, Development of Bismuth ferrite as a piezoelectric and multiferroic material by cobalt substitution, Adv. Mater. 30 (2018) 1705665.
[48] R.M. Bozorth, E.F. Tilden, A.J. Williams, Anisotropy and magnetostriction of some ferrites, Phys. Rev. 99 (1955) 1788–1798.
[49] K. Venkata Siva, S. Sudersan, A. Arockiarajan, Bipolar magnetostriction in CoFe2O4: effect of sintering, measurement temperature, and prestress, J. Appl. Phys. 128 (2020) 103904.
[50] J. Neubert, S. Wagner, J.C.W. Kiwit, A.U. Bräuer, J. Glumm, New findings about iron oxide nanoparticles and their different effects on murine primary brain cells, Int. J. Nanomed. 10 (2015) 2033–2049.
[51] X. Valentini, P. Deneufbourg, P. Paci, P. Rugira, S. Laurent, A. Frau, D. Stanicki, L. Ris, D. Nonclercq, Morphological alterations induced by the exposure to TiO2 nanoparticles in primary cortical neuron cultures and in the brain of rats, Toxicol. Rep. 5 (2018) 878–889.
[52] J. Lojk, L. Babič, P. Sušjan, V.B. Bregar, M. Pavlin, I. Hafner-Bratkovič, P. Veranič, Analysis of the direct and indirect effects of nanoparticle exposure on microglial and neuronal cells In vitro, Int. J. Mol. Sci. 21 (19) (2020) 7030, 21.
[53] T.H. Shin, D.Y. Lee, Y.E. Jang, D.H. Kwon, J.S. Hwang, S.G. Kim, C. Seo, M.J. Paik, J.Y. Lee, J.Y. Kim, S. Park, S.-E. Choi, S. Basith, M.O. Kim, G. Lee, Reduction in the migration activity of microglia treated with silica-coated magnetic nanoparticles and their recovery using Citrate, Cells 11 (15) (2022) 2393, 11.
[54] M. Linnerbauer, M.A. Wheeler, F.J. Quintana, Astrocyte crosstalk in CNS inflammation, Neuron 108 (2020) 608–622.

[55] J.W. Salatino, K.A. Ludwig, T.D.Y. Kozai, E.K. Purcell, Glial responses to implanted electrodes in the brain, Nat. Biomed. Eng. 1 (2018) 862–877.
[56] F. Darlot, P. Villard, L.A. Salam, L. Rousseau, G. Piret, Glial scarring around intracortical MEA implants with flexible and free microwires inserted using biodegradable PLGA needles, Front. Bioeng. Biotechnol. 12 (12) (2024) 1408088.
[57] A. Rodzinski, R. Guduru, P. Liang, A. Hadjikhani, T. Stewart, E. Stimphil, C. Runowicz, R. Cote, N. Altman, R. Datar, S. Khizroev, Targeted and controlled anticancer drug delivery and release with magnetoelectric nanoparticles, Sci. Rep. 6 (2016) 20867.
[58] H. Song, D. Kim, S.A. Abbasi, N. Latifi Gharamaleki, E. Kim, C. Jin, S. Kim, J. Hwang, J.-Y. Kim, X.-Z. Chen, B.J. Nelson, S. Pané, H. Choi, Multi-target cell therapy using a magnetoelectric microscale biorobot for targeted delivery and selective differentiation of SH-SY5Y cells via magnetically driven cell stamping, Mater. Horiz. 9 (2022) 3031–3038.
[59] T. Janusas, S. Urbaite, A. Palevicius, S. Nasiri, G. Janusas, Biologically compatible lead-free piezoelectric composite for acoustophoresis based particle manipulation techniques, Sensors 21 (2) (2021) 483, 21.
[60] Stephen F Larner, Jonathan Wang, Jared Goodman, Megan B O'Donoghue Altman, Meiguo Xin, Kevin K W Wang, Vitro neurotoxicity resulting from exposure of cultured neural cells to several types of nanoparticles, J. Cell Death. 10 (2017) 1179670717694523.
[61] A. Haase, S. Rott, A. Mantion, P. Graf, J. Plendl, A.F. Thünemann, W.P. Meier, A. Taubert, A. Luch, G. Reiser, Effects of silver nanoparticles on primary mixed neural cell cultures: uptake, oxidative stress and acute calcium responses, Toxicol. Sci. 126 (2012) 457–468.
[62] A. Kaushik, R.D. Jayant, R. Nikkhah-Moshaie, V. Bhardwaj, U. Roy, Z. Huang, A. Ruiz, A. Yndart, V. Atluri, N. El-Hage, K. Khalili, M. Nair, Magnetically guided central nervous system delivery and toxicity evaluation of magneto-electric nanocarriers, Sci. Rep. 6 (2016) 25309.
[63] M. Nair, R. Guduru, P. Liang, J. Hong, V. Sagar, S. Khizroev, Externally controlled on-demand release of anti-HIV drug using magneto-electric nanoparticles as carriers, Nat. Commun. 4 (2013) 1707.
[64] K.L. Kozielski, A. Jahanshahi, H.B. Gilbert, Y. Yu, Ö. Erin, D. Francisco, F. Alosaimi, Y. Temel, M. Sitti, Nonresonant powering of injectable nanoelectrodes enables wireless deep brain stimulation in freely moving mice, Sci. Adv. 7 (2021) eabc4189.
[65] S. Kemppainen, N. Huber, R.-M. Willman, A. Zamora, P. Mäkinen, H. Martiskainen, M. Takalo, A. Haapasalo, T. Sobrino, M.A. González Gómez, Y. Piñeiro, J. Rivas, U. Himmelreich, M. Hiltunen, Organotypic hippocampal slice cultures from adult tauopathy mice and theragnostic evaluation of nanomaterial phospho-TAU antibody-conjugates, Cells 12 (2023) 1422, 10.
[66] M. Pohland, R. Glumm, F. Wiekhorst, J. Kiwit, J. Glumm, Biocompatibility of very small superparamagnetic iron oxide nanoparticles in murine organotypic hippocampal slice cultures and the role of microglia, Int. J. Nanomed. 12 (2017) 1577–1591.
[67] J. Ji, A. Moquin, F. Bertorelle, P.K.Y Chang, R. Antoine, J. Luo, R.A. McKinney, D. Maysinger, Organotypic and primary neural cultures as models to assess effects of different gold nanostructures on glia and neurons, Nanotoxicology 13 (2019) 285–304.
[68] Y. Cheng, Q. Dai, R.A. Morshed, X. Fan, M.L. Wegscheid, D.A. Wainwright, Y. Han, L. Zhang, B. Auffinger, A.L. Tobias, E. Rincón, B. Thaci, A.U. Ahmed, P.C. Warnke, C. He, M.S. Lesniak, Blood-brain barrier permeable gold nanoparticles: an efficient delivery platform for enhanced malignant glioma therapy and imaging, Small 10 (2014) 5137–5150.
[69] J.K. Saucier-Sawyer, Y. Deng, Y.-E. Seo, C.J. Cheng, J. Zhang, E. Quijano, W. M. Saltzman, Systemic delivery of blood–brain barrier-targeted polymeric nanoparticles enhances delivery to brain tissue, J. Drug Target. 23 (2015) 736–749.
[70] J. Chen, M. Yuan, C.A. Madison, S. Eitan, Y. Wang, Blood-brain barrier crossing using magnetic stimulated nanoparticles, J. Control. Release 345 (2022) 557–571.
[71] L. Horev-Azaria, G. Baldi, D. Beno, D. Bonacchi, U. Golla-Schindler, J. C. Kirkpatrick, S. Kolle, R. Landsiedel, O. Maimon, P.N. Marche, J. Ponti, R. Romano, F. Rossi, D. Sommer, C. Uboldi, R.E. Unger, C. Villiers, R. Korenstein, Predictive toxicology of cobalt ferrite nanoparticles: comparative in-vitro study of different cellular models using methods of knowledge discovery from data, Part Fibre Toxicol. 10 (2013) 32.
[72] E. Akinci, R. Köylü, M. Yortanli, H. Gümüş, Ö. Köylü, L. Altintepe, B. Cander, Acute bismuth intoxication: acute renal failure, tonsillar ulceration and posterior reversible encephalopathy syndrome, Hong Kong J. Emerg. Med. 22 (2015) 121–125.
[73] B.A. Fowler, D.W. Sullivan, M.J. Sexton, Chapter 31 - bismuth, in: G.F. Nordberg, B.A. Fowler, M. Nordberg (Eds.), Handbook On the Toxicology of Metals (Fourth Edition), Academic Press, San Diego, 2015: pp. 655–666.
[74] A. Atwal, G.C.S. Cousin, Bismuth toxicity in patients treated with bismuth iodoform paraffin packs, Br. J. Oral Maxillofac. Surg. 54 (2016) 111–112.
[75] A. Marino, S. Arai, Y. Hou, E. Sinibaldi, M. Pellegrino, Y.-T. Chang, B. Mazzolai, V. Mattoli, M. Suzuki, G. Ciofani, Piezoelectric nanoparticle-assisted wireless neuronal stimulation, ACS Nano 9 (2015) 7678–7689.
[76] K.L. Kozielski, A. Jahanshahi, H.B. Gilbert, Y. Yu, Ö. Erin, D. Francisco, F. Alosaimi, Y. Temel, M. Sitti, Nonresonant powering of injectable nanoelectrodes enables wireless deep brain stimulation in freely moving mice, Sci. Adv. 7 (2022) eabc4189.
[77] E. Zhang, M. Abdel-Mottaleb, P. Liang, B. Navarrete, Y.A. Yildirim, M.A. Campos, I. T. Smith, P. Wang, B. Yildirim, L. Yang, Magnetic-field-synchronized wireless modulation of neural activity by magnetoelectric nanoparticles, Brain Stimul. 15 (2022) 1451–1462.
[78] L. He, Z. Sun, J. Li, R. Zhu, B. Niu, K.L. Tam, Q. Xiao, J. Li, W. Wang, C.Y. Tsui, Electrical stimulation at nanoscale topography boosts neural stem cell neurogenesis through the enhancement of autophagy signaling, Biomaterials 268 (2021) 120585.
[79] Y. Zhang, S. Chen, Z. Xiao, X. Liu, C. Wu, K. Wu, A. Liu, D. Wei, J. Sun, L. Zhou, Magnetoelectric nanoparticles incorporated biomimetic matrix for wireless electrical stimulation and nerve regeneration, Adv. Heal. Mater. 10 (2021) 2100695.